magenta

Low-Cost Melt Pool Monitoring in Wire Arc Additive Manufacturing

A Thesis Presented for the

Master of Science in Mechanical Engineering

Degree

The University of Tennessee, Knoxville

Steven Grant Wilmoth

May 2025

© by Steven Grant Wilmoth, 2025
All Rights Reserved.

Acknowledgments

I would like to thank Dr. Bradley Jared for allowing me to further my education and explore new and exciting technologies in a hands-on environment. Thank you to Steven Williams, Devon Goodspeed, Tiffany Quigley, and Matthew Roach for their invaluable support in helping me learn to weld, conduct experiments, analyze data, and operate the equipment essential for my research. Finally, thank you to Andrej Nycz at ORNL, Dustin Wagner at Miller, and all the other sponsors of the Ma2JIC Program that gave the funding and guidance needed to make my research possible.

Abstract

Wire-Arc Additive Manufacturing (WAAM) is an emerging metal manufacturing technology that utilizes welding processes to build large-scale components in significantly reduced timeframes at lower costs with less material waste. However, maintaining consistent part quality remains a challenge due to variations in weld bead size, shape, and overall deposition characteristics. The enclosed research explores the development of a low-cost melt pool monitoring solution using readily available and inexpensive hardware and open-source software to analyze the deposition process and identify observable weld characteristics from an optical camera feed.

The system's effectiveness was evaluated by testing various weld parameters, introducing controlled defects, and using different materials to assess the correlation between melt pool behavior and process conditions. Post-processing of the recorded frame data was conducted using a combination of traditional image analysis techniques and machine learning algorithms to extract data on weld features and establish relationships between weld parameters and visual melt pool characteristics.

The final camera system utilized a neutral density filter and low exposure times to mitigate the arc flash from the deposition process. The melting of the welding wire into the melt pool, the solidification front, and the arcflash itself were visible in the video frames. These components were detected by a machine learning algorithm and the data about their size and location within the video feed were used to compare the differences in the feed when weld parameters were changed.

Table of Contents

1 Introduction **1**

1.1 Introduction to Wire-Arc Additive Manufacturing 1

1.2 Deposition Physics 3

1.3 WAAM Process Difficulties and Motivation for In-Situ WAAM Monitoring . 6

1.4 GMAW Monitoring Challenges 7

2 Prior Research **8**

3 Experimental Methods **10**

3.1 Experimental Approach 10

3.2 WAAM Equipment 11

3.2.1 WAAM Deposition Hardware 11

3.2.2 Wire and Substrate Material. 11

3.2.3 Path Planning 15

3.2.4 Deposition Process 17

3.3 Camera Equipment 17

3.3.1 Basler Optical Camera System 17

3.3.2 Adjustable Camera Mount Design 20

3.3.3 Camera Filters 24

3.3.4 Data Acquisition and Script Development 26

3.4 Development of Imaging Conditions 27

3.4.1 Optimal vs. Sub Optimal Deposits 28

3.4.2 Neutral Density Filters and Exposure Times 31

3.4.3 Wavelength Pass Band Filters . . . 34
3.4.4 Investigation of Low-Cost External Illumination . . . 41
3.4.5 Optimal Camera Settings . . . 41
3.5 Image Analysis . . . 45
3.5.1 Pixel Segmentation . . . 45
3.5.2 Machine Learning Based Segmentation . . . 47
3.6 Process Changes, Defects, and Part Monitoring . . . 49
3.6.1 Deposition Parameter Variations . . . 49
3.6.2 Deposition Defect Introduction . . . 51
3.6.3 Constant Heat Input With Varying Deposition Parameters . . . 51
3.6.4 Part Monitoring . . . 51

4 Results and Discussion **53**
4.1 Correlation Between Heat Input, Solidification Zone Size, and Wire Area. . . 53
4.2 Deposition Defect Correlation . . . 56
4.3 Deposition Images with Same Heat Input . . . 61
4.4 Demonstration of WAAM Part Monitoring . . . 65

5 Conclusions and Recommendations **69**

Bibliography **71**

Vita **79**

List of Tables

3.1 Optimal settings used for material deposition 29

3.2 Optimized Camera and Filter Settings 42

3.3 Deposition settings for heat input testing, 410 SS material, 6.35 mm/s travel speed. 50

3.4 Deposition settings for heat input testing, 316 LSI SS material, 5.08 mm/s travel speed. 50

3.5 Deposition defect parameters used to observe differences in defective depositions compared to optimal settings seen in table 3.1. 52

3.6 Constant heat input parameters for 316 LSI SS material. Used to observe differences in deposition images with changing wire feed speed and travel speed while maintaining heat input of 360 J/mm. 52

4.1 Four test conditions from 4.1 of variable wire feed speed settings tested with a 0.8 OD ND filter applied. 55

List of Figures

1.1 KUKA KR-6 WAAM development cell used for deposition and experimentation. 2
1.2 Wire arc printing of a marine propeller. [1] 2
1.3 WAAM build constructed with deposition layers in quick succession, resulting in overheating. 5

3.1 WAAM setup with Kuka KR6, Fronius CMT VR 7000 Wire feeder, Fronius CMT 4000 power supply, fixture table, shielding gas, Basler camera, and controlling computer[2] 12
3.2 Kuka KR6 and Fronius welding torch WAAM deposition setup. 12
3.3 Fronius CMT VR 7000 power supply for WAAM deposition 13
3.4 Camera mount and Fronius Robacta Drive CMT W assembly. 13
3.5 Universal mount with Picatinny rails [3]. 14
3.6 Rhino and Grasshopper path plan with sliced box example. 16
3.7 Prepared 1018 mild steel substrate 18
3.8 Basler camera and lens assembly used in study 18
3.9 Welding clamps used in WAAM deposition 19
3.10 Basler ace acA800-200gc spectral response chart[4] 21
3.11 Basler camera mount design. 21
3.12 22.5°, 33.75°, and 45° viewing angles. 22
3.13 Distance definitions for camera setup 23
3.14 22.5 degree viewing angle of 6061 aluminum WAAM deposition. 25
3.15 6061 aluminum deposits with optimal deposition conditions described in Table 3.1 29

3.16 6061 aluminum deposits generated with no shielding gas and unprepared substrate. 29
3.17 Steel WAAM deposition with porosity. 30
3.18 Examples of a 6061 RAM Al depositions with discontinuities. 30
3.19 Effect of increasing exposure time with the same ND filter selection. 32
3.20 Effect of using a darker ND filter with the same exposure time. 33
3.21 First trial of exposure time changes for 316 LSI SS. Camera setting development. 35
3.22 Second trial of exposure time changes for 316 LSI SS. Camera setting development. 36
3.23 Third trial of exposure time changes for 316 LSI SS. Camera setting development. 37
3.24 316 LSI SS final camera setting histogram. 38
3.25 Effect of applying 752nm bandpass filter to camera system on 410 SS WAAM deposition. 39
3.26 Effect of applying 875nm longpass filter to camera system on 410 SS WAAM deposition. 40
3.27 External illumination setup with camera system. 42
3.28 Effect of applying 20,000 lumen external illumination to 6061 Al deposition process. 43
3.29 Selected camera settings applied to ideal deposition conditions. 44
3.30 Threshold pixel analysis on WAAM deposition. 46
3.31 Object class outlining procedure. 48
3.32 Object class outlining procedure. 48

4.1 Effect of increasing the wire feed speed on the images seen by the camera system on 410SS WAAM deposition. 54
4.2 Effect of increasing the wire feed speed on the images seen by the camera system on 316SS WAAM deposition. 54
4.3 Evident solidification zone and welding wire pixel area trends with changes in heat input for 316 LSI SS material. 57

4.4 Evident solidification zone and welding wire pixel area trends with changes in heat input for 410SS material. 58
4.5 Large spatter streaks visible in video feed. 59
4.6 Erratic behavior seen in deposition defect conditions. 60
4.7 Effect on pixel area with shielding gas removed for 410 SS. slightly different feature area, much higher standard deviation. 62
4.8 Effect on pixel area seen by model with shielding gas removed and lower heat input for 6061 RAM Al. Much smaller feature area detected with change in standard deviation for arc flash area. 63
4.9 No clear change in pixel area detected by model with constant heat input settings. 64
4.10 Change in location of deposition location in camera system feed after 18 layers of deposition. 66
4.11 316 LSI part from part monitoring experiment. 66
4.12 Part build in positive Y direction showing strong trend in location change versus layer number. 68

Chapter 1

Introduction

1.1 Introduction to Wire-Arc Additive Manufacturing

Wire-Arc Additive Manufacturing (WAAM) is a Direct Energy Deposition (DED) technique that has emerged as a suitable alternative for medium-to-large scale part production [5, 6]. However, WAAM is a relatively new manufacturing technique and is still under heavy development and evolution. WAAM typically utilizes a Gas Metal Arc Welding (GMAW) torch mounted on a controlled motion system, generally a six-axis robotic manipulator, to precisely deposit material layer by layer. The process begins by striking an electric arc onto a substrate, melting the wire feedstock into the resulting melt pool, and moving the welding torch in a controlled manner. The process, ideally, creates a bead that is consistent in length and shape. Successive layers are then built upon the initial deposition, gradually forming a near-net-shape three-dimensional part meant for further machining to meet final tolerances and geometries. Two samples of these can be seen in Figure 1.1 and Figure 1.2.



Figure 1.1: KUKA KR-6 WAAM development cell used for deposition and experimentation.



Figure 1.2: Wire arc printing of a marine propeller. [1]

WAAM has several advantages over other additive manufacturing methods. A WAAM setup can be made with a commercially available robotic manipulator, a welding power supply, and a GMAW torch with shielding gas. The shielding gas cools the deposition process and ensures that having an inert enclosure is not required, unlike laser and electron beam powder bed fusion manufacturing. WAAM is also significantly lower in time costs compared to traditional manufacturing, as it utilizes feedstock wire instead of large castings to produce parts. In addition, the deposition rate for WAAM can be as high as 160g/min whereas laser and electron beam powder bed additive manufacturing are roughly 2-10g/min [6], drastically reducing manufacturing time for large-scale parts. Thanks to these advantages, WAAM is widely applicable in maritime [7], aerospace [8], and other industries.

1.2 Deposition Physics

Deposition bead quality and resultant strength are inherently linked to process parameters within the deposition process [9]. Key factors such as welding voltage, current, wire feed speed, and shielding gas flow rate play a critical role in determining the properties and performance of the final weld [9, 10]. A lower wire feed speed reduces deposition and heat input, resulting in a smaller solidification front trailing the melt pool area while increasing the risk of defects such as insufficient fusion with underlying layers [11]. An excessively high wire feed speed may lead to excessive heat input, altering the cooling rate of the material and affecting the final weld shape [12]. Additionally, the arc area serves as an indicator of energy input and heat distribution. When viewing it with an optical monitoring system, a smaller arc flash may indicate that the melting wire is partially obscuring the arc, suggesting that the wire is melting too slowly or other problems. The solidified material area provides insight into deposition uniformity and cooling behavior. A larger solidification zone with the same heat input suggests excessive heat accumulation in the underlying layers or substrate, which can result in defects such as poor bead geometry [12] or poor interlayer bonding. An example of this can be seen in Figure 1.3, where a build was performed with deposition layers happening in quick succession, which caused overheating in the part. Additionally, the area of the welding wire visible to the camera can provide an understanding of changing

process parameters. A decrease in the visible length of the welding wire protruding past the nozzle, suggests a greater heat input from a change in amperage or a reduction in deposition travel speed. This could potentially lead to burn-through due to excessive heat. [13]. By establishing metrics at which these physical parameters define an optimal deposition under ideal process conditions, these indicators can be systematically compared against various deposition conditions to identify deviations that may lead to suboptimal results.



Figure 1.3: WAAM build constructed with deposition layers in quick succession, resulting in overheating.

1.3 WAAM Process Difficulties and Motivation for In-Situ WAAM Monitoring

Despite its advantages, the widespread adoption of WAAM is limited by challenges in maintaining process stability and achieving consistent geometric accuracy. The manufacturing of a part is closely tied to the dynamic fluid behavior of the melt pool, which is heavily influenced by key process parameters such as welding current, voltage, travel speed, welding angle, and wire feed speed [14]. Improper parameters, environmental factors, changes in heat dissipation, wear on consumables, and changes in material properties can lead to defects including oxidation, lack of fusion, porosity, and slag inclusion [15, 16, 17, 18]. These defects can accumulate with each layer, cascading degrading geometric accuracy and material properties until the part becomes unusable. To maintain high quality and minimize defects, real-time monitoring and control strategies are essential [19].

Several methods exist for collecting the deposition data needed for any type of real-time monitoring and process control, including high-frequency sampling of welding voltage and current [20], and laboratory-grade welding cameras capable of capturing highly detailed and clear melt pool images [21, 22, 23]. However, often these solutions are expensive and require specialized software, hardware, and integration systems, further increasing the barrier to entry for small and mid-sized manufacturers. Additionally, manufacturing environments are harsh, exposing the sensitive equipment to extreme heat, spatter from the deposition process, and other harmful conditions. The potential failure, repair, or replacement of expensive sensors from any damage caused by the environment further compounds the challenges associated with integrating WAAM into large-scale production. Developing a low-cost melt pool monitoring system with off-the-shelf hardware and open-source software would significantly reduce both initial and ongoing costs associated with WAAM. The goal of this project is to provide an accessible solution for deposition monitoring to accomplish these objectives. The successful implementation of this system would not only reduce overhead costs but also improve efficiency by providing a way to monitor the deposition process to alert the operator for any defects or other issues, saving time and resources. Ultimately, this

research aims to contribute to making WAAM a more viable and scalable manufacturing technology for a broader range of industries.

1.4 GMAW Monitoring Challenges

Observing a GMAW welding arc with an optical camera presents a significant challenge due to the extreme brightness and spectral range of the arc flash [24]. The light emission, which spans both visible and infrared wavelengths, overwhelms standard camera sensors designed for normal lighting conditions, resulting in images that are saturated and provide an essentially featureless white flash. Camera options capable of mitigating the brightness of the welding arc during deposition are expensive because of their specialized sensors capable of handling extreme contrasts. The cameras often employ ultraviolet (UV) and infrared (IR) cut filters to remove any non visible wavelengths from the video feed, such as the Xiris-1100 [25]. Some cameras utilize an external illumination source, typically a laser, that is brighter than the arc flash but limited to a specified wavelength. By employing a bandpass filter on the camera that only allows light at the external illumination wavelength to pass through, the arc flash's overwhelming intensity is balanced, enabling a clearer view of the deposition process, such as the solidification front, wire, and melt pool. An example of this is Cavitar C300, which employs a 640nm class 3R laser for melt pool illumination [26]. Other options include thermal cameras that only view the melt pool with IR wavelengths. The two types include Near-IR (NIR) and Short-Wave IR (SWIR), such as the Xiris XVC750 and the Xiris XIR-1800, respectively. The Xiris XIR-1800 utilizes an InGaAs optical sensor due to the higher sensitivity in the 900 to 1700nm wavelength range [27] for detailed images in temperatures exceeding 500°C, and a normal CMOS sensor is used in the Xiris XVC750 NIR thermal camera for basic thermal imaging [28].

Chapter 2

Prior Research

Monitoring of the melt pool in a WAAM process through visual methods is difficult due to the strong arc light and high temperatures present during the deposition process [29, 30, 31]. To counteract the brightness of the arc flash and the difficulty in viewing the deposition process, a variety of industrial welding camera solutions combined with post-process analysis through the use of image segmentation and varying neural network algorithms have been deployed with promising and accurate prediction of deposition defects and geometry.

Dong et. al [30] successfully used a Xiris XVC-500 welding camera, a 670nm +/-20 bandpass filter, a 10% transmittance attenuator, and a UV lens in a weld reinforcement and bead trend prediction study. They employed a deposition pool contour extraction algorithm and mathematical model from the video feed that had 0.55% error in dimensional measurements between measured and predicted weld reinforcement. They proved that the mathematical model they formed between welding process parameters and weld pool contour dimensions can be used to analyze the quality of deposition shape in the process of additive manufacturing that improved the deposition forming accuracy.

Wang et. al [31] used a hybrid combination of the images from a Xiris XVC-1000 welding camera and voltage signals to identify defects in lap MIG welding. The data was collected using a synchronized trigger to align melt pool images with simultaneously captured voltage signals. A Short-time Fourier Transform was then applied to explore frequency variations in the voltage data. Then, the time spectrogram and molten pool image were fed into a hybrid

Convolutional Neural Network (CNN) model to detect a normal welding state and four types of defects: arcing, weld bias, burn-through, and uneven width, with a 98.87% accuracy.

Franke et. al [19] used a Cavitar C300 and a neural network based semantic segmentation method, a type of model that classifies each pixel to a defined object class, to identify WAAM defects. The images from the Cavitar camera were used to monitor the nozzle to workpiece distance and horizontal position of the wire during welding. Extensive efforts were made using traditional image analysis to detect spatter on the deposition image using connected component analysis (CCA). They successfully used this system to monitor the nozzle to workpiece distance (dNtW) despite the rapidly changing lighting conditions, proving this method is suitable for maintaining dNtW based monitoring of the deposition process.

Xia et. al [21] investigated various deep learning methods on the images from a Xiris XVC-1000E to prove that CNN models are effective in classifying certain melt pool defects in WAAM. Humping, spattering, and robot suspend (unintentional decrease in speed or stop in travel) defects were intentionally introduced into the deposition process, and the images from the welding camera during these defects were analyzed using various CNN architectures. The results proved that CNN models are very effective at detecting humping, spattering, and robot suspend deposition defects, with accuracies of 97.25%, 97.15%, 97.62% and 97.45% obtained by GoogLeNet, VGG-16, ResNet, and EfficientNet respectively.

Although successful in each endeavor, these studies rely on expensive welding cameras to remove or drastically reduce the arc flash from the images of the melt pool for any defect or process change monitoring. Various post-processing was accomplished to achieve different desired outcomes, but the incorporation of the respective welding camera is a requirement for any further implementation of any study. To explore if monitoring WAAM deposition is only possible through the welding camera implementation, this study aims to explore similar melt pool viewing and defect detection, but through the use of a low-cost camera and easily accessible software. The implementation of such a system would decrease the barrier of entry for small to medium scale manufacturers by reducing overall manufacturing costs, system costs, and adding defect detection methods.

Chapter 3

Experimental Methods

3.1 Experimental Approach

Keeping the process difficulties associated with WAAM in mind and the previous attempts at using high-cost cameras to control them, a low-cost and easily accessible monitoring solution capable of capturing melt pool dynamics needs to have a suitable optical camera, lens, adjustable mount, and optical filters capable of mitigating the GMAW arc flash. To accomplish this, first identifying and acquiring a suitable camera system comprising of both a low-cost sensor and suitable lens. Then, a robust mounting system that would allow for flexible positioning and optimal viewing angles of the melt pool was designed and fabricated. Controlled deposition experiments were then conducted to capture camera-feed images under stable and unstable deposition process conditions on a development system. The resulting data was analyzed to determine the extent to which process changes and defects can be identified through the low-cost novel method. Finally, image processing techniques were applied to correlate melt pool characteristics and deposition conditions to determine whether the image feed results can be used for WAAM deposition defect monitoring.

3.2 WAAM Equipment

3.2.1 WAAM Deposition Hardware

The WAAM equipment used for this research, seen in Figure 3.1, is a GMAW welding setup with a Fronius VR 7000 CMT wire feeder, Fronius CMT 4000 power supply, and Fronius Robacta Drive CMT W gas metal arc welding (GMAW) end effector mounted to a Kuka KR6 robotic manipulator, seen in Figure 3.2 and Figure 3.3. The Kuka KR6 is a low payload six-axis manipulator used in wire arc applications [32]. The Fronius VR 7000 CMT wire feeder is a 4 roll drive wire feeder for all types of MIG/MAG welding[33]. The Fronius VR 4000 power supply is a microprocessor-controlled welding power source featuring an maximum output of 400 A [34]. The Fronius Robacta Drive CMT W GMAW welding torch is a gas-cooled welding torch typically seen in WAAM applications [35]. To mount sensors to the welding torch, a universal sensor mounting system previously developed for other research was used, as seen in Figure 3.4. It features aluminum cross-supports with milled aluminum Picatinny rails [3], securely bolted to a circular baseplate that is mounted to the robot's end effector. The design enables the attachment of various sensor configurations with multiple rigid anchor points, as shown in Figure 3.5

3.2.2 Wire and Substrate Material.

Three different deposition wire materials were utilized during experiments, 6061 RAM aluminum, a proprietary aluminum wire produced by Fortius Metals [36], 410 stainless steel (SS), and 316 stainless steel. These materials were chosen because of their alignment with other ongoing research, and allowed camera capabilities to be tested and developed. The substrate materials used were 1018 mild steel plates for the stainless steel feedstock and 6061 aluminum plates for the 6061 RAM al feedstock. Each substrate was 6in wide by 12in long by 0.5in thick.

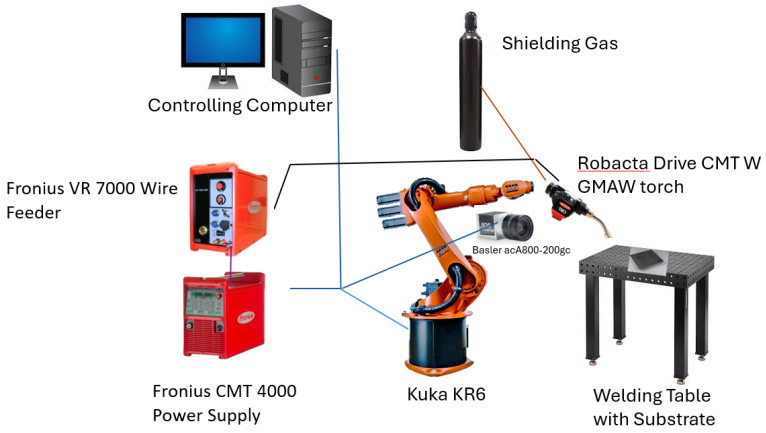


Figure 3.1: WAAM setup with Kuka KR6, Fronius CMT VR 7000 Wire feeder, Fronius CMT 4000 power supply, fixture table, shielding gas, Basler camera, and controlling computer[2]



Figure 3.2: Kuka KR6 and Fronius welding torch WAAM deposition setup.

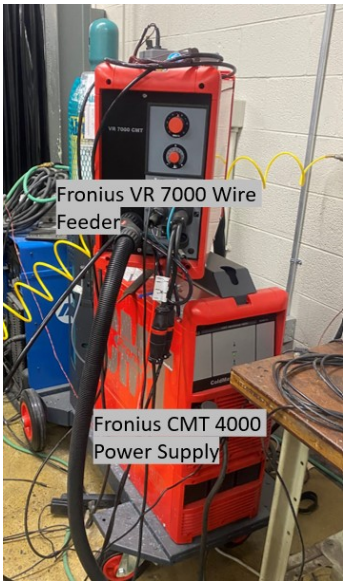


Figure 3.3: Fronius CMT VR 7000 power supply for WAAM deposition

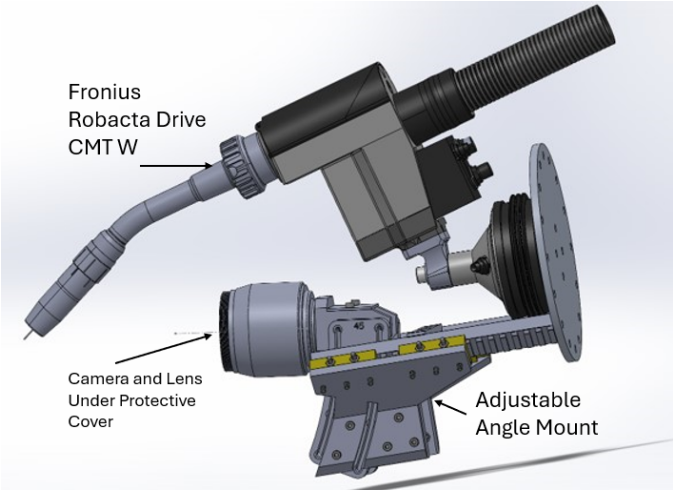


Figure 3.4: Camera mount and Fronius Robacta Drive CMT W assembly.

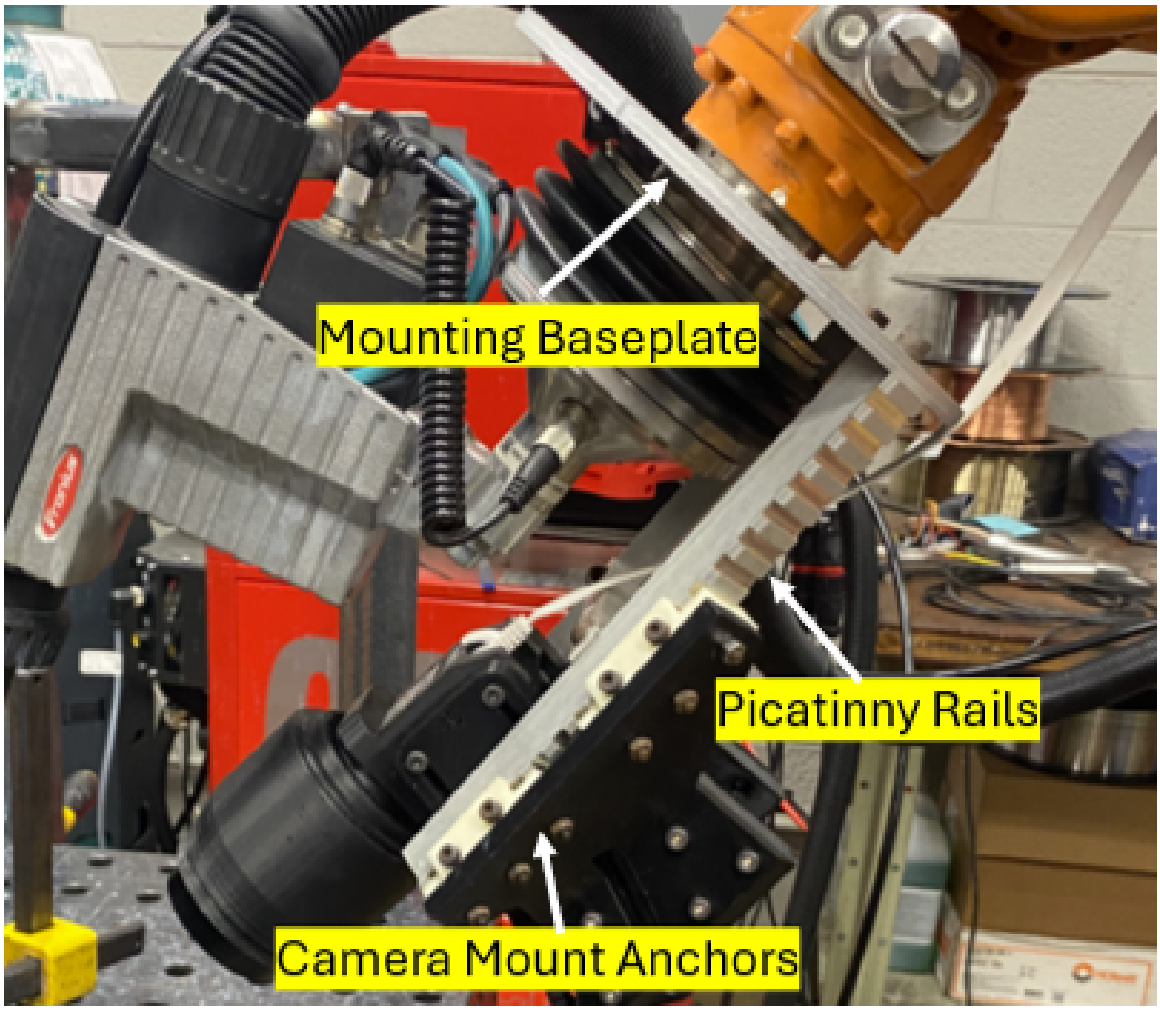


Figure 3.5: Universal mount with Picatinny rails [3].

3.2.3 Path Planning

Path planning for the robot to perform the deposition operations was done using two methods. The first was a custom path plan generation setup in Rhinoceros 7 [37] and its accompanying parametric scripting environment, Grasshopper, as seen in Figure 3.6. In this program, parts of desired geometry were sliced using a method of interpolating planes from the baseplate to one slightly above the part and solving for the intersection of the part and the planes. The resultant intersection curves were divided into points and frames were assigned to each one to designate tool orientation, with the KukaPRC plugin for Grasshopper assigning a path plan for the Kuka to the points and exporting the code for direct use on the KR6. The Grasshopper path planning method is best for complex geometries but for simple one directional deposition beads, it is more efficient to use an alternate method, manually programming motion with the pendant.

Programming the paths manually using the Kuka's teaching pendant was the most frequently used path planning method. Paths were created by moving the robot manually with the pendant until the welding nozzle was in the desired position with the correct contact tip to workpiece distance (CTWD). The initial deposition point was then recorded using the ArcOn command with the Kuka ArcTech plugin. Then, the robot was moved until the nozzle was at the end of the deposition bead with the same CTWD and the end point was set with the ArcOff command.

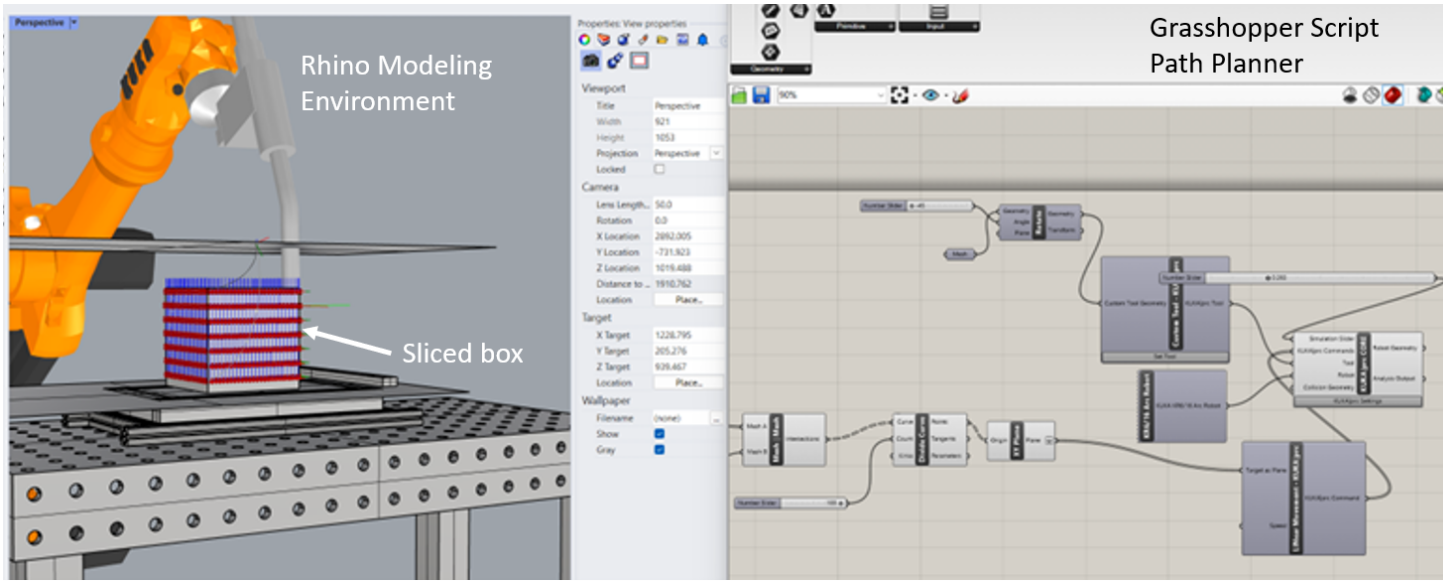


Figure 3.6: Rhino and Grasshopper path plan with sliced box example.

3.2.4 Deposition Process

Each build plate was prepared for WAAM deposition by grinding the surface with an 80-grit flap disc attached to an angle grinder and by then cleaning with acetone and paper towels. The cleaning process removed any surface coatings that the substrates were shipped with and allows for greater adhesion of the deposited material. Once the substrate was prepared, it was placed onto the development cell's welding table and clamped securely down with steel clamps. Such clamping ensured a conductive pathway for the power supply and to prevent shifting or warping as the WAAM deposition cools and shrinks.Smaller fixtures were used to prevent the plate from moving on the table, and the larger clamps were used to act as another method of keeping the substrate in place but also to prevent the deposition substrate from deforming while the deposited bead cooled, Figure 3.9. Every subsequent bead was then made in reference to the first, adjusting each ArcOn and ArcOff point by moving them in the x or y direction depending on where the next deposition bead would be located. The distance was generally 20mm from the start of the previous deposit in the -x direction, perpendicular to the bead length, until all available space on the substrate was used. A sample prepared 1018 mild steel substrate with the path planning coordinate system can be seen in Figure 3.7.

3.3 Camera Equipment

3.3.1 Basler Optical Camera System

The camera selected for this study was a Basler acA800-200gc optical camera (Figure 3.8) due to its proven use with the project collaborators at Oak Ridge National Laboratory (ORNL). The camera is able to capture frames at a rate of 240 frames per second, its operational settings can be programmed through scripting software, communicates using the GigE interface, and it is a low cost camera, at only $529.00 [4]. It has a 800 x 600 pixel resolution, and produces images with a bit depth of 10 bits for better color accuracy [38, 39].

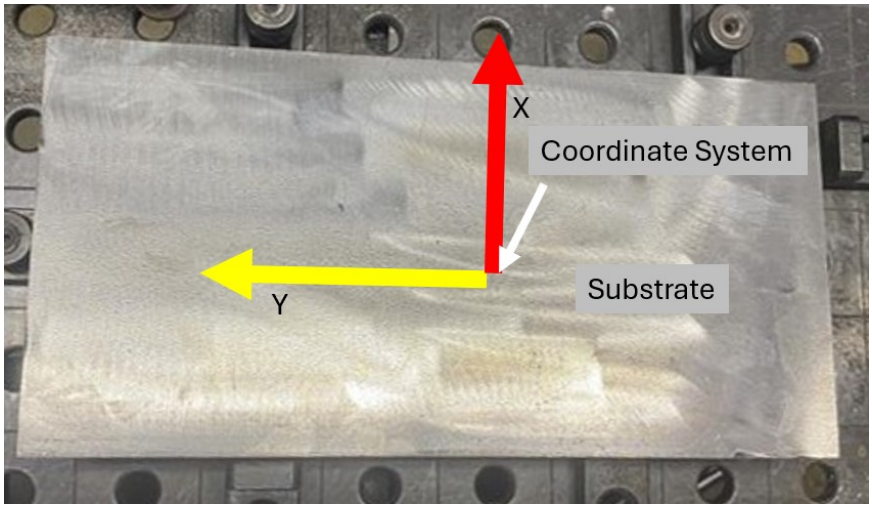


Figure 3.7: Prepared 1018 mild steel substrate



Figure 3.8: Basler camera and lens assembly used in study

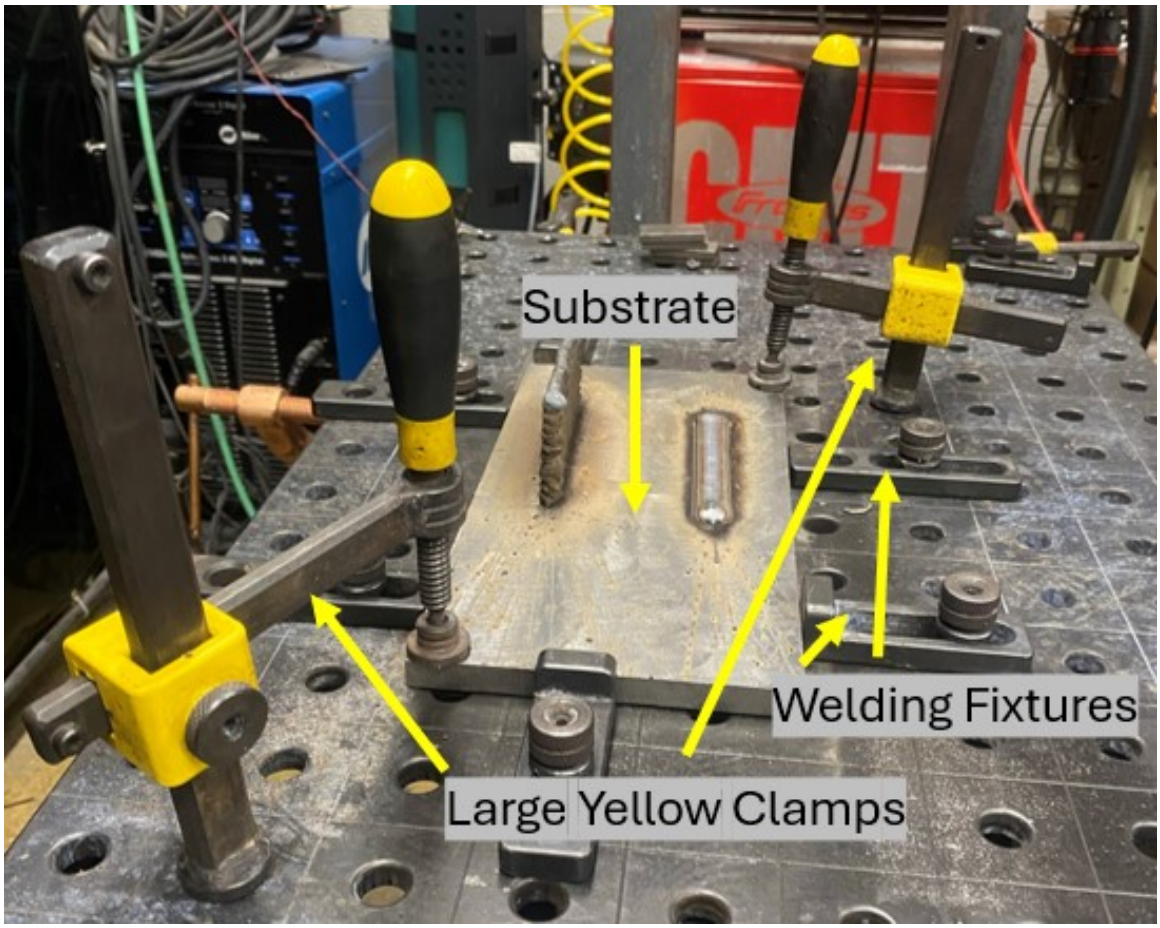


Figure 3.9: Welding clamps used in WAAM deposition

The camera's spectral response plot, seen in Figure 3.10, shows that it is capable of capturing images of the deposition process across both visible and near-infrared (NIR) wavelengths.

The accompanying lens chosen for the camera was the C12-2524-25M-P[40]. The lens has a fixed focal length 25mm, has manual iris control, has a working distance of 150mm, and operates across the entire visible wavelength spectrum [38]. It mounts to the Basler sensor using a C-mount, and it includes an adjustable aperture and iris.

3.3.2 Adjustable Camera Mount Design

Properly mounting the camera required a mount that was both adjustable in angle and rigid in construction. Adjustability of the viewing angle ensured that all critical components of the deposition process remained within the field of view, while a rigid setup minimized any vibrations that could affect image quality. Additionally, a secure mount helps maintain consistent object centering and focus settings across different deposition trials, improving the reliability of the data collection. The camera mount that was designed can be seen in Figure 3.11. It was fused deposition model (FDM) printed out of ASA for durability and heat resistance. The design of the mount allowed for adjustable angle viewing of the melt pool. The viewing angle could be adjusted from 22.5° to 45° relative to the substrate surface. Figure 3.12 showcases sample image feeds capturing the deposition process from different viewing angles. In this case, when the contact tip-to-work distance (CTWD) is reduced, a narrower viewing angle is required to clearly observe the deposition, as the gas nozzle partially obstructs the view within the frame, emphasizing the importance of the adjustable viewing angle the camera mount offers. A set of covers for the sensor and lens was also printed to protect the camera system from radiant heat from the deposition process and any spatter that could land on it. The material used for the prints was ASA for its higher mechanical strength and heat resistance. The Camera Distance (CD) from the lens to the tip of the feedstock wire, seen in Figure 3.13, was standardized to 150mm.

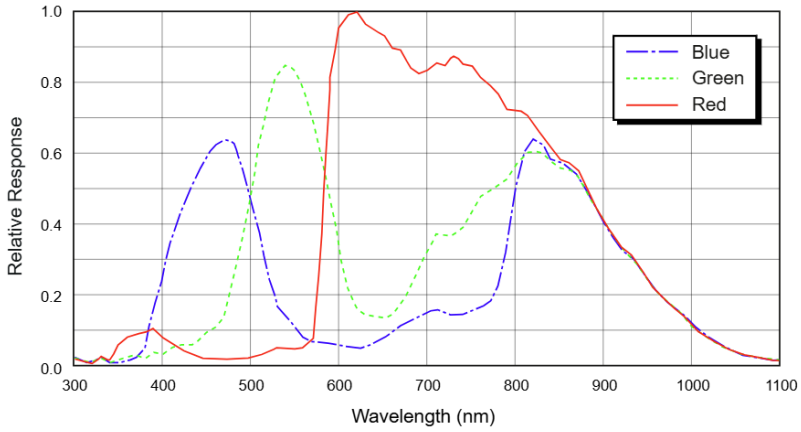


Figure 3.10: Basler ace acA800-200gc spectral response chart[4]

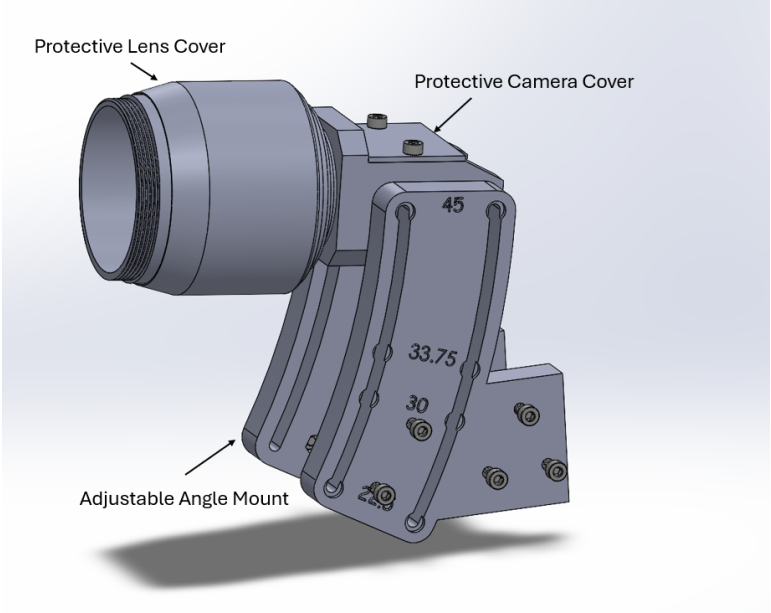
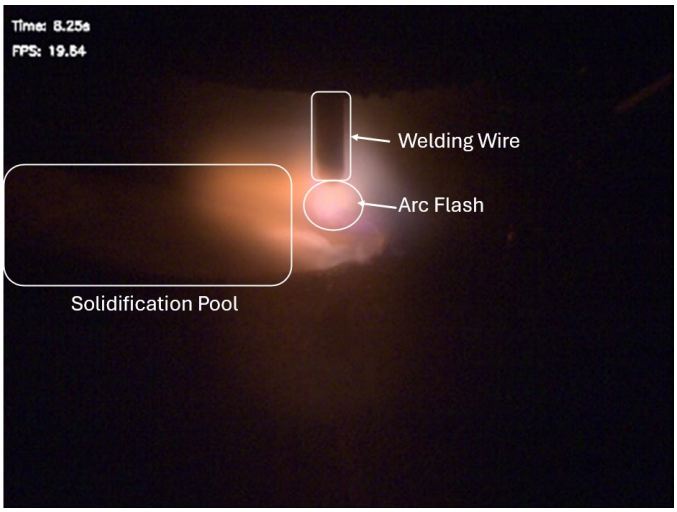
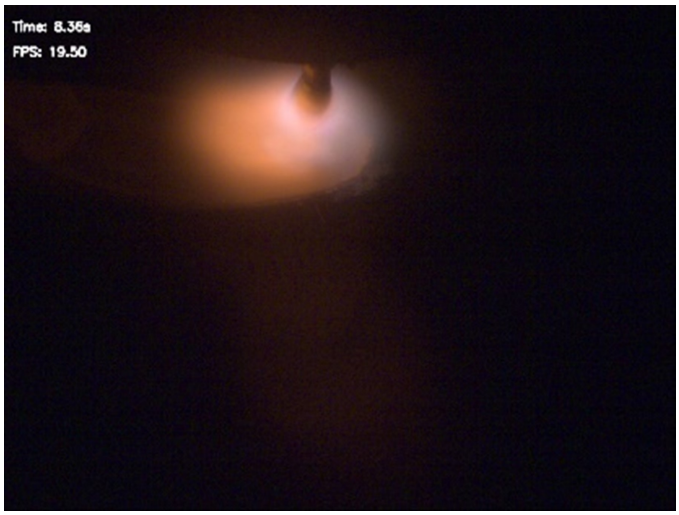


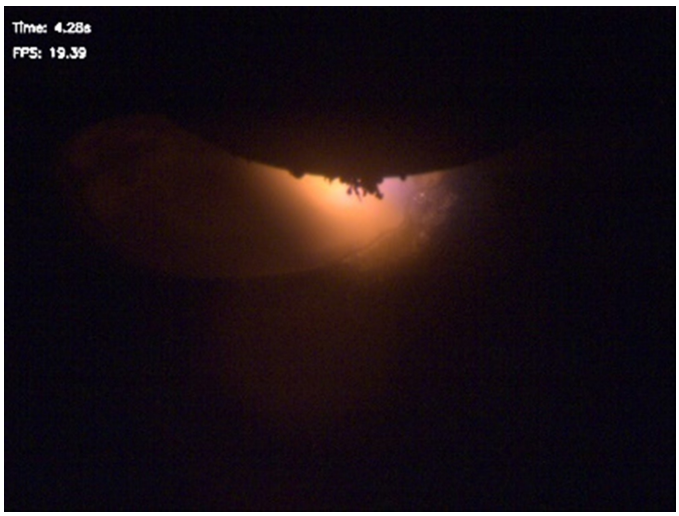
Figure 3.11: Basler camera mount design.



(a) 22.5°



(b) 33.75°



(c) 45°

Figure 3.12: 22.5°, 33.75°, and 45° viewing angles.

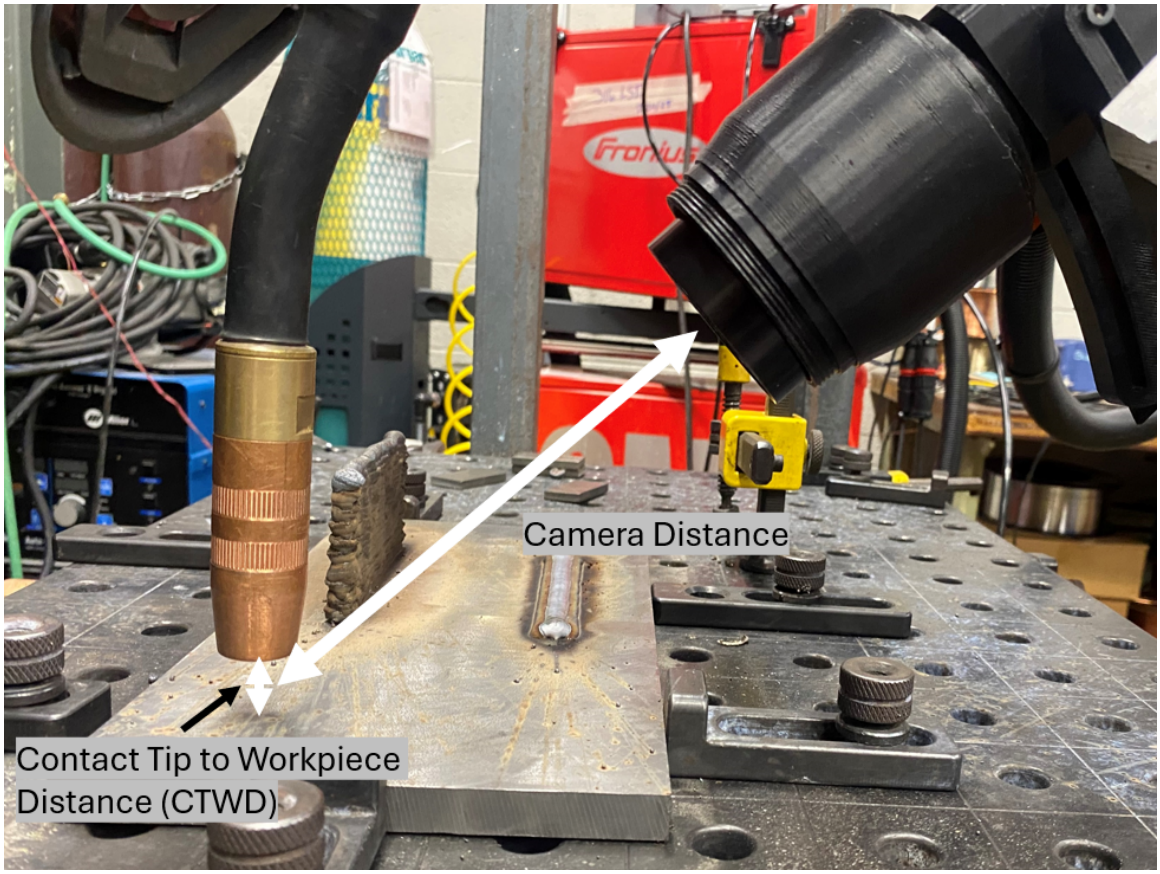


Figure 3.13: Distance definitions for camera setup

The original design goal of the camera mount was to have viewing angles from 0° to 45. However, several design constraints emerged. Extending the mount for viewing below 22.5° relative to the substrate surface introduced collision potential with the substrate and its holding clamps. Furthermore, analysis of the images of the mounting system in use indicated that angles below approximately 22.5° did not capture a sufficient portion of the solidification zone, seen in Figure 3.14, limiting its viability and utility.

One alternative camera mounting approach that was considered involved utilizing off-the-shelf modular camera link systems that incorporated adjustable ball mounts, knuckles, and couplers [41]. However, this method was ultimately deemed unsuitable due to the challenges it would introduce in maintaining a consistent and repeatable camera viewing position and angle, which is critical for accurate data collection.

3.3.3 Camera Filters

Three different types of optical filters were selected and employed to address the challenges of WAAM deposition monitoring: neutral density filters, bandpass filters, and longpass filters.

A neutral density (ND) filter greatly attenuates the intensity of the light reaching the camera sensor, reducing the intensity of the arc flash such that melt pool features can be imaged [42]. ND filters are described using a logarithmic scale following the relationship:

$$OD = -log(\frac{T}{100\%}) \tag{3.1}$$

where OD is the optical density of the filter and T denotes the percent transmittance of the light [43]. Three different ND optical filters were used with ODs of 0.8 OD, 1.5 OD, and 4.0 OD. With the logarithmic scale of the formula, this corresponds to the filters have a percent transmittance of 15.8%, 3.2%, and 0.01%, respectively. Arc flashes from a GMAW welding process can be between 10,000 and 300,000 lumens [44]. Adding a 4.0 OD filter with a 0.01% transmittance to the camera feed reduces the incoming light transmittance from 100,000 to 1,000 lumens, which is comparable to a 10W LED bulb[44].

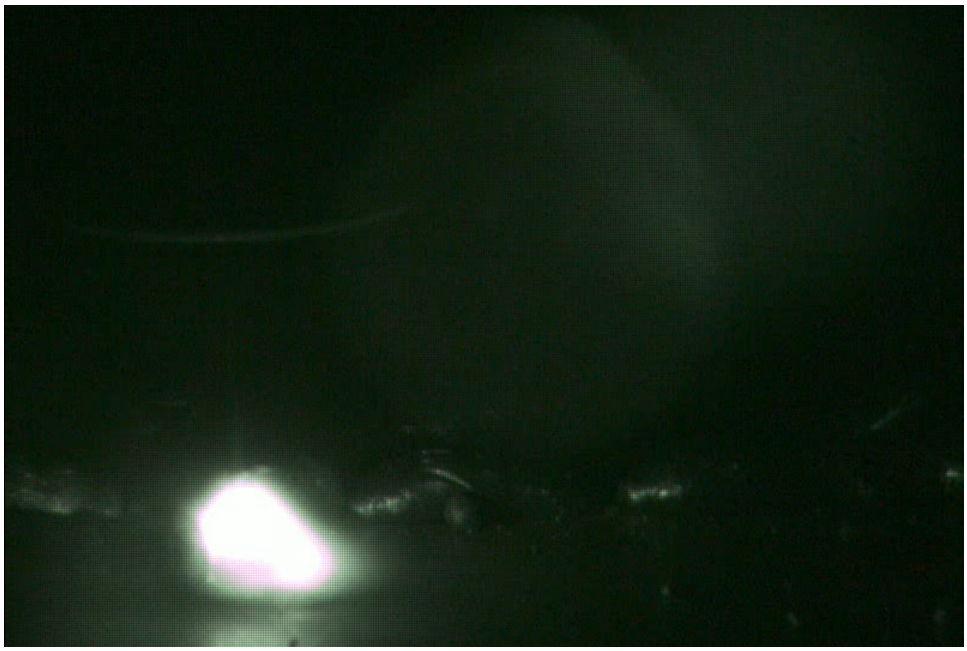


Figure 3.14: 22.5 degree viewing angle of 6061 aluminum WAAM deposition.

A bandpass filter was selected to narrow the spectral range seen by the camera sensor. These types of filters only pass light with wavelengths within a narrow, specified range, i.e., its bandpass, while blocking all other wavelengths. The filter selected was a 752nm ± 10nm filter. The chosen wavelength was selected for several reasons. The chosen wavelength was selected for several reasons. First, the arc flash emits light over a range of wavelengths, with certain wavelengths having significantly higher intensity than others [24]. By filtering out the wavelengths where the arc flash is most intense, its overwhelming brightness is reduced, improving visual imaging. Second, previous research suggests that melt pool for stainless steel is visible within the 752nm ± 10nm wavelength range [45]. Lastly, this filter was readily available from previous research efforts.

A longpass optical filter was evaluated in addition to the bandpass filter. Longpass filters allow wavelengths longer or equal to than a specified wavelength to pass through the filter and therefore enter the camera sensor. In this case, a 875nm longpass filter was selected based on previous studies that had shown that melt pool visibility for stainless steel via optical imaging was clearest at that wavelength and above. [45]

3.3.4 Data Acquisition and Script Development

Initial camera setup and operation leveraged the Pylon Viewer provided for free by Basler for focus adjustments, connectivity verification, and further troubleshooting.

To facilitate real-time image acquisition and control of the camera system, custom Python scripts were developed using Basler's PyPylon library. PyPylon provides the ability to control and capture frames with the Basler camera through a GigE interface. It further allows for dynamic adjustments of the camera settings from the controlling computer such as gain, framerate, and most importantly, exposure time, as the camera records. These functions were crucial for experiment efficiency by allowing multiple capture conditions to be tested within a single deposition operation.

Script development began with simple video recordings of the deposition process but gradually expanded in scope as data collection progressed and desired results and tracking needs became clearer. The first major improvement involved implementing dynamic exposure time adjustments within the script, allowing exposure to change during video collection. By

enabling dynamic exposure times in each video, melt pool images were captured at multiple exposure levels within a single deposition process, significantly increasing the efficiency of data collection. Next, annotations were incorporated into the videos to track video feed details including time elapsed, frames per second, material type, applied filters, and exposure settings. A raw video file without the annotations was also saved for image analysis. These annotations were later expanded to include additional parameters such as shielding gas type, external illumination settings, camera model, lens specifications, aperture and focus settings, and the viewing angle of the melt pool. To allow for more detailed frame information, the script was then modified to capture individual frames instead of full videos, saving the frames sequentially with associated metadata instead of combining them all into a single video with annotations. Finally, integration with the Kuka Robot Sensor Interface (RSI) was implemented by detecting the deposition signal available within the real-time RSI data packet. Implementing this change eliminated the need for manual camera activation, eliminating the blank data recorded before and after the deposition process associated with manual starting and ending of the script, and reduced file size.

3.4 Development of Imaging Conditions

Developing the camera settings is the most crucial step in the data collection process. Without a properly tuned imaging system, meaningful data acquisition would be impossible. A systematic approach was applied across all materials and involved optimizing exposure time, filters, and viewing angle to balance the light intensity from the arc flash to be able to view important aspects of the deposition. The goal was to view the solidification zone, the welding wire, the shape of the arc flash, and any other identifiable objects in the video feed.

3.4.1 Optimal vs. Sub Optimal Deposits

The classification of deposition quality varies depending on the specific application and material. However, for this study, a deposition with optimal settings is defined as one that maintains consistent and controlled bead geometry, as seen in Figure 3.15. Critical defects that must be avoided include porosity, cracking, excess oxidation, or discontinuities (as seen in Figure 3.18), that can greatly compromise the mechanical strength and substrate tie-in of the deposition bead, as seen in Figure 3.16 and 3.17

Optimal deposition parameters for this study were determined based on previous research and ongoing projects involving the materials mentioned in 3.2.2. The established settings are summarized in Table 3.1, where WFS is the Wire Feed Speed, TS is the Travel Speed, and HI is the Heat Input. The CTWD was standardized to 15mm. Current and voltage values were recorded from the Fronius power supply control pendant, though these values fluctuate depending on deposition conditions and should be considered approximate due to droplet transfer and changes in arc length [46].

Current and voltage are influenced by wire feed speed, with higher values correlating to increased heat input. Heat input is a critical factor in WAAM deposition, as it directly impacts cooling rates, penetration depth, deposition rate, and deposition bead size. It is calculated using Equation 3.2, where the thermal efficiency for GMAW welding is estimated to be 0.8 [47].

$$\text{Heat Input (J/mm)} = \frac{\text{Voltage (V)} * \text{Current (A)}}{\text{Travel Speed (mm/s)}} * \text{Thermal Efficiency} \tag{3.2}$$

Because heat input is a ratio-dependent function, different deposition settings can yield the same heat input. For instance, reducing current and voltage lowers heat input, but if travel speed is also reduced proportionally, the overall heat input remains unchanged. Changing the proportion to maintain a constant heat input is useful for testing slower deposition speeds.

Table 3.1: Optimal settings used for material deposition

Material	Current (A)	Voltage (V)	WFS (mm/s)	TS (mm/s)	HI (J/mm)
6061 RAM Al	143	20.9	201.1	3.38	706
410 SS	154	20.6	88.9	6.35	399.7
316 LSI SS	178	14.3	93.1	5.08	400.9



Figure 3.15: 6061 aluminum deposits with optimal deposition conditions described in Table 3.1

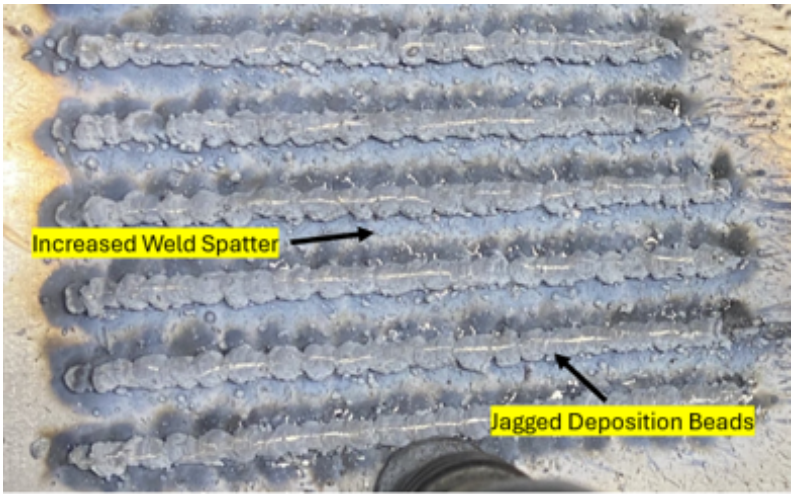


Figure 3.16: 6061 aluminum deposits generated with no shielding gas and unprepared substrate.

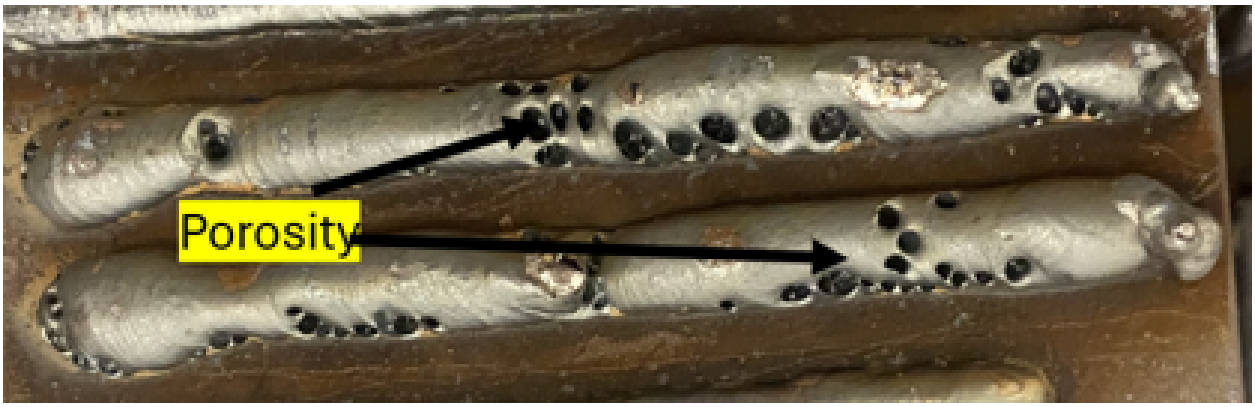


Figure 3.17: Steel WAAM deposition with porosity.

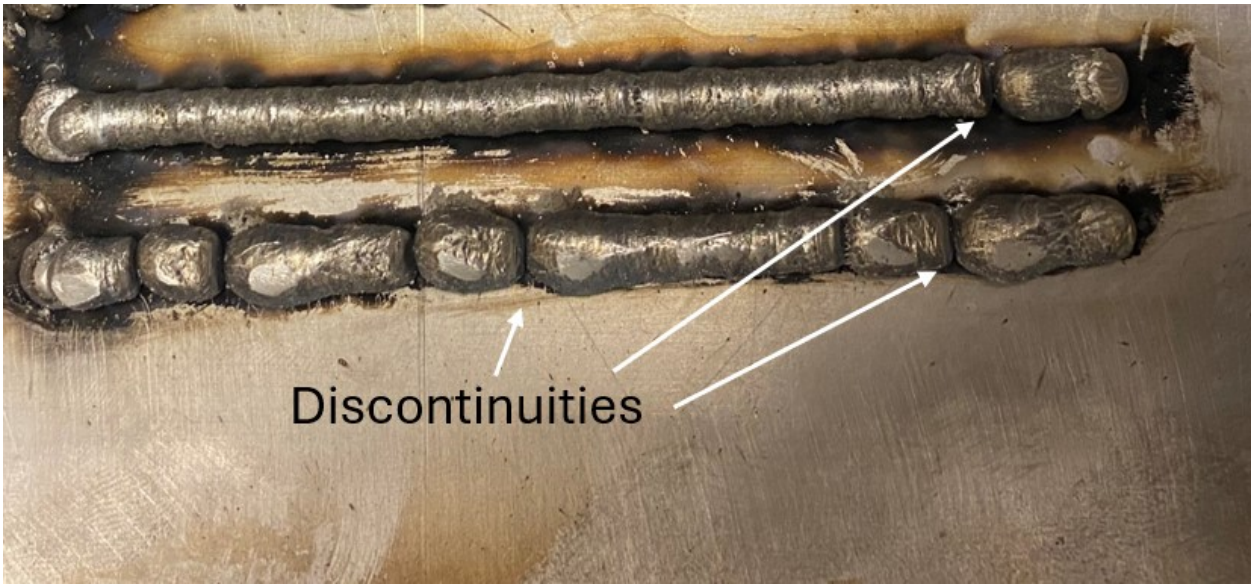
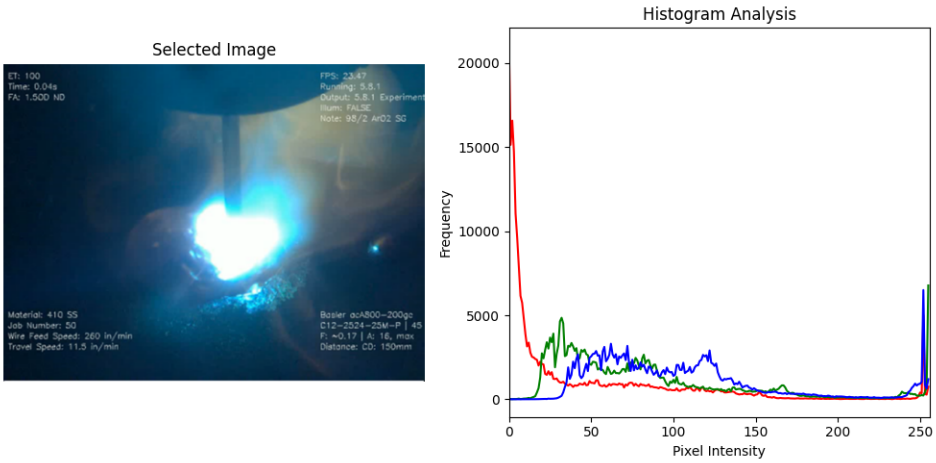


Figure 3.18: Examples of a 6061 RAM Al depositions with discontinuities.

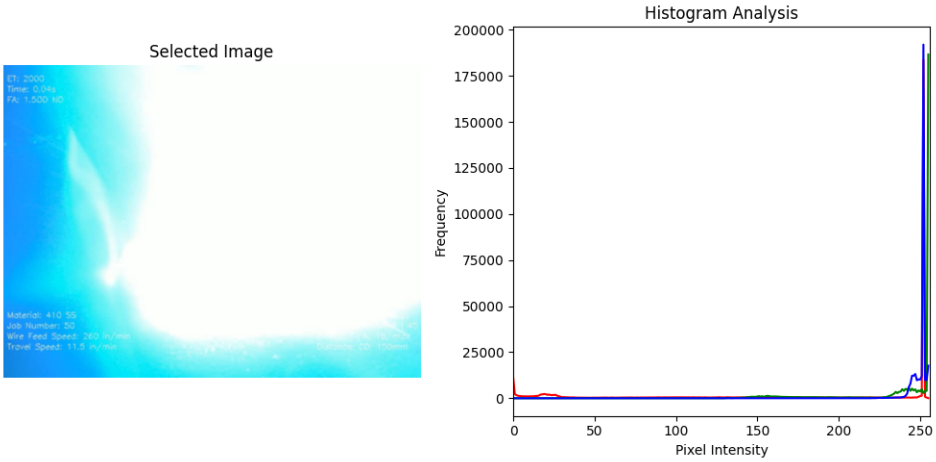
3.4.2 Neutral Density Filters and Exposure Times

The selection of appropriate ND filters and camera exposure time played the most critical role in optimizing the clearest view of the welding deposition. ND filters reduce the intensity of incoming light by reducing the welding arc's brightness while increasing or decreasing the exposure rate subsequently reduces or increases light levels reaching the camera sensor during the frame capture. If using an ND filter with relatively high transmittance results in image washout, a lower-transmittance filter could be applied to mitigate the exposure, or the exposure time could be reduced to lower the amount of light entering the camera sensor during the frame capture, seen in Figure 3.19. Conversely, if the captured video appears too dim from the selected ND filter, a higher transmittance ND filter could be applied or the exposure time increased to allow more light into the sensor during the frame capture, seen in the comparison in Figure 3.20. Balancing both factors is crucial, as the arc flash is too bright to capture without an ND filter, even with the shortest exposure time on the camera. However, using an ND filter with the lowest transmittance would necessitate a longer exposure time to capture a useful frame, resulting in a frame rate too low to use for monitoring.

The method for testing the neutral density filters and exposure time for the optimal solution was to first run a deposition test with the lightest available neutral density filter, the 0.8 OD ND filter. The deposition was completed with active data collection while simultaneously changing the exposure time of the camera in seven intervals over a large range, usually from 80μS to 0.5s. The video was then observed, and the exposure time range where the arc flash was best mitigated was then divided further into seven additional segments and the experiment repeated. The process was iterated to determine the optimal exposure time for the associated neutral density filter, typically requiring three-four repetitions of the experiment. If the arc intensity was not mitigated sufficiently in any of the exposure time ranges with the lightest neutral density filter, the experiment was repeated with a darker, more restrictive neutral density filter, and the exposure time experiment was repeated.

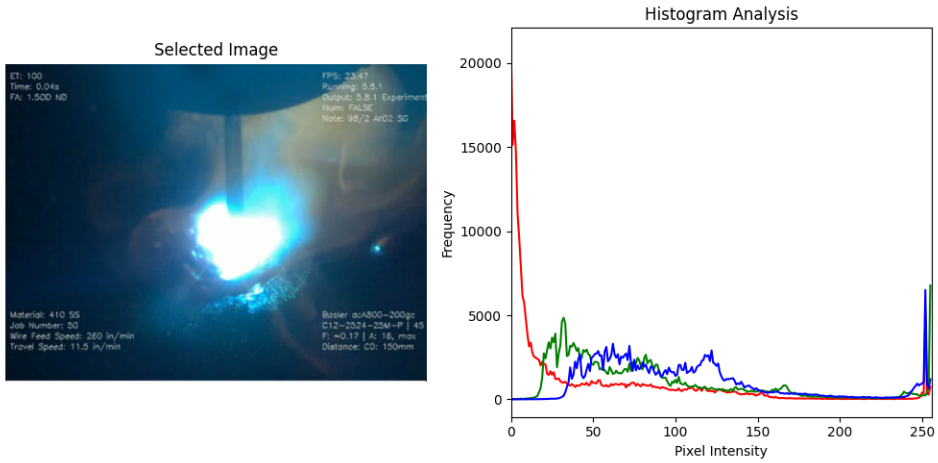


(a) 1.5 OD ND filter applied, 0.1ms exposure time, 410SS material.

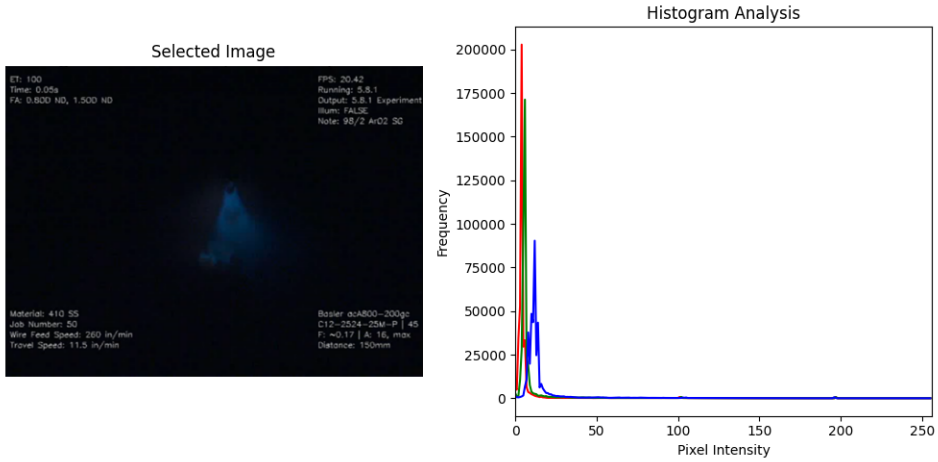


(b) 1.5 OD ND filter applied, 2.0ms exposure time, 410SS material.

Figure 3.19: Effect of increasing exposure time with the same ND filter selection.



(a) 1.5 OD ND filter applied, 0.1ms exposure time, 410SS material.



(b) 1.5 OD ND and 0.8 OD ND filter applied, 0.1ms exposure time, 410SS material.

Figure 3.20: Effect of using a darker ND filter with the same exposure time.

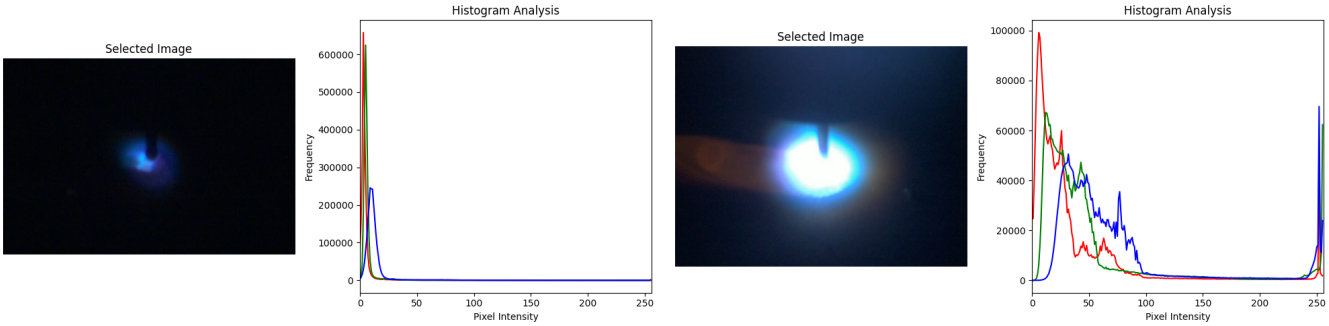
Quantitatively, this process is shown by the histogram charts seen in Figure 3.21, Figure 3.22, and Figure 3.23, with the final camera setting selection seen in Figure 3.24. The arc flash brightness is best mitigated when the highest-intensity pixels are eliminated while still allowing enough light to illuminate the other objects in the deposition process. As a result, sufficient data can be collected from the video feed.

3.4.3 Wavelength Pass Band Filters

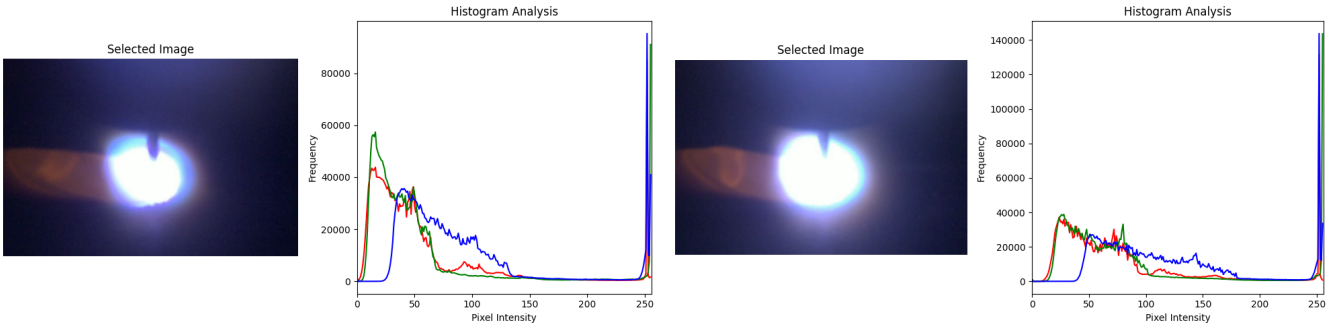
To test the available optical filters for deposition viewing, the filters were tested in combination with the selected optimal exposure time and neutral density filters with the same deposition parameters and conditions. The goal was to determine if the application of the optical filters mitigated the arc flash to an acceptable level.

The 752nm bandpass filter significantly dims the image, rendering the captured frames too dark to extract meaningful information, seen in Figure 3.25. Increasing the exposure time for this filter was also explored to obtain clearer images of the deposition. However, in order to achieve the same visibility as the images with only ND applied, the exposure time needed to be increased exponentially, decreasing the framerate and data collection speed to an impractical level.

Conversely, the 875nm longpass filter introduces noticeable blurring with no significant change between the feed with the applied filter and without, seen in Figure 3.26. Given these limitations, neither filter was viable for continued use in data collection.

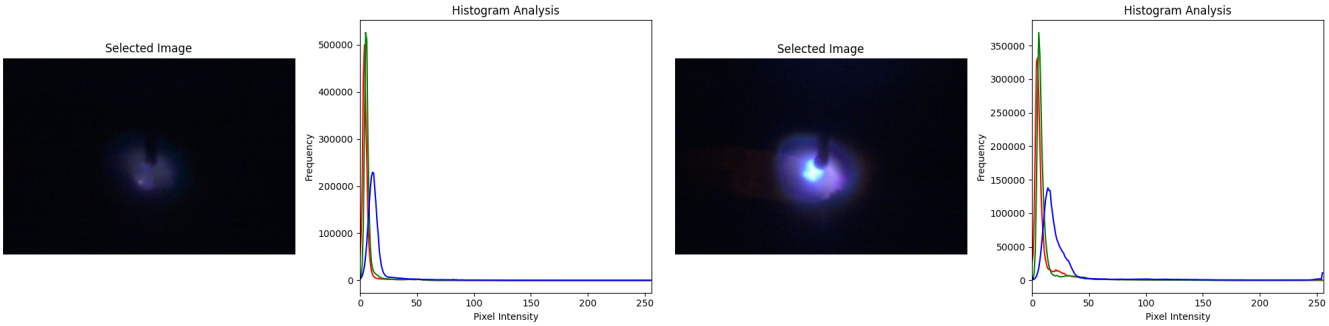


(a) 80μS ET **(b)** 7580μS ET

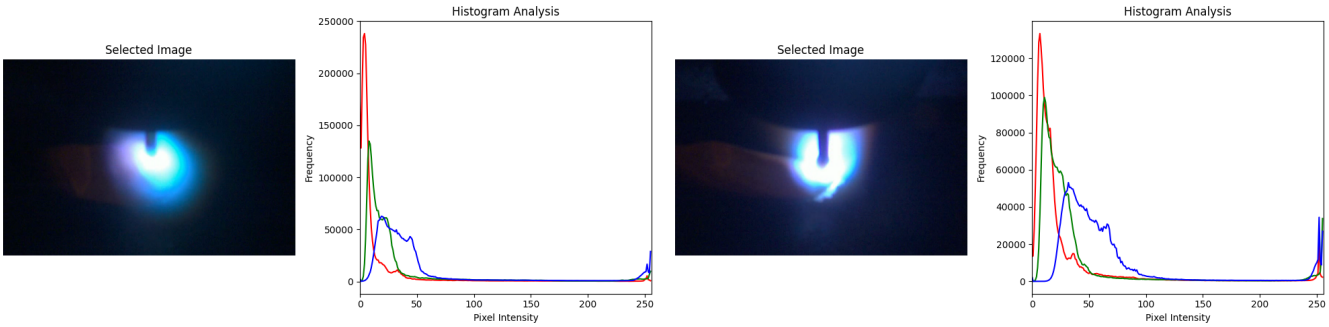


(c) 15080μS ET **(d)** 22580μS ET

Figure 3.21: First trial of exposure time changes for 316 LSI SS. Camera setting development.

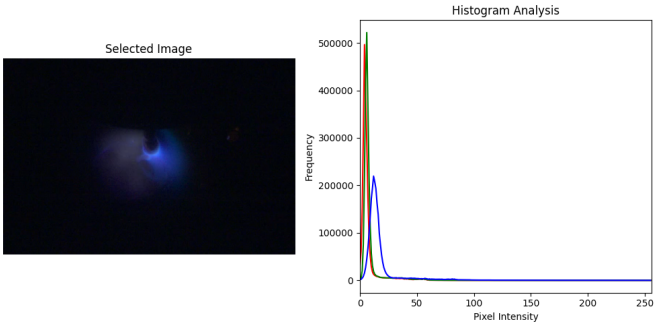


(a) 80μS ET **(b)** 1080μS ET

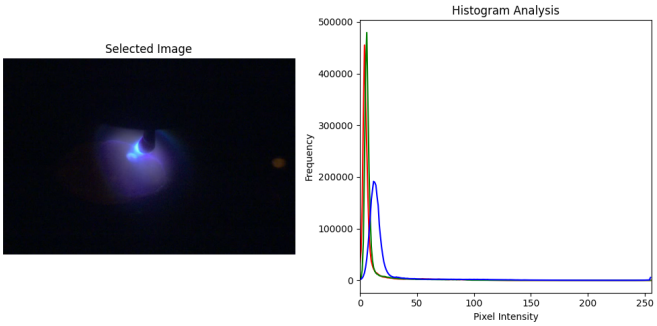


(c) 2080μS ET **(d)** 3080μS ET

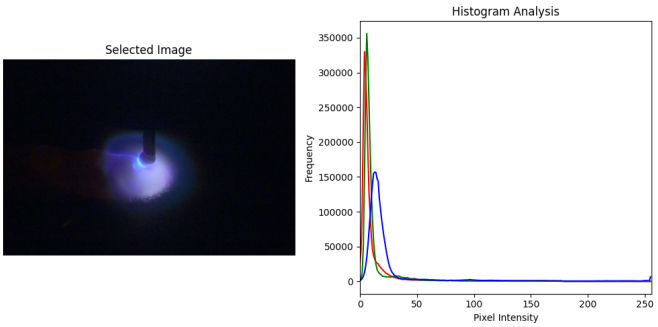
Figure 3.22: Second trial of exposure time changes for 316 LSI SS. Camera setting development.



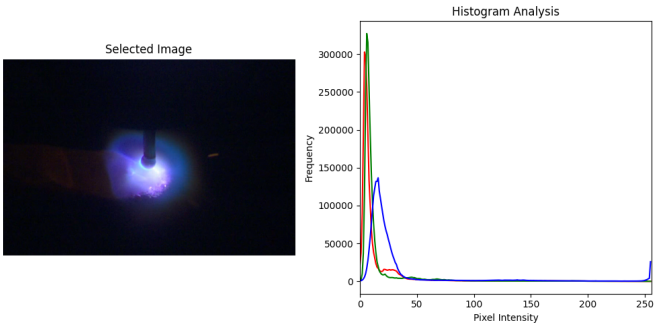
(a) 80μS ET



(b) 520μS ET



(c) 960μS ET



(d) 1400μS ET

Figure 3.23: Third trial of exposure time changes for 316 LSI SS. Camera setting development.

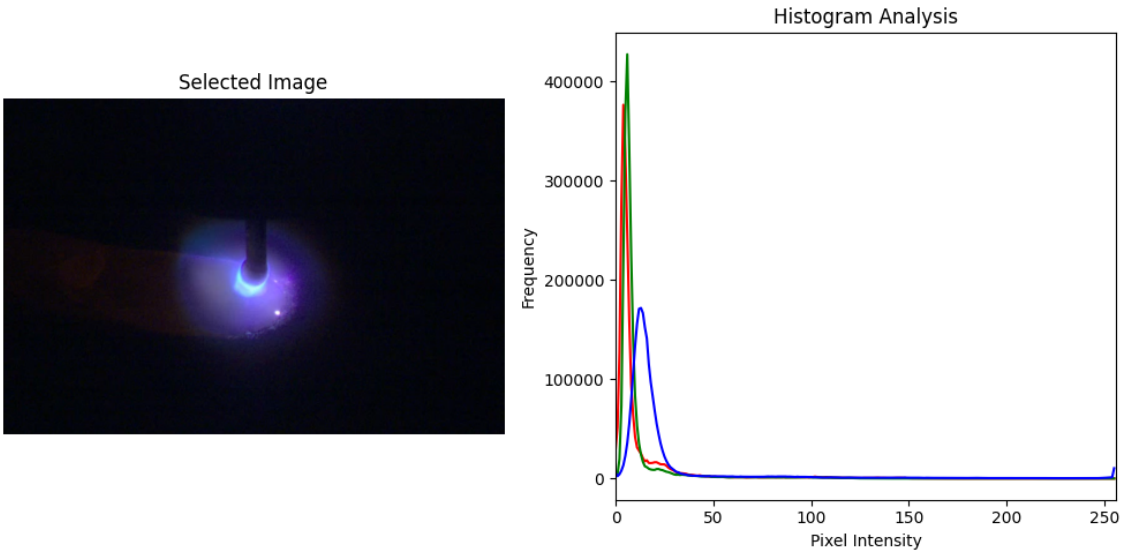
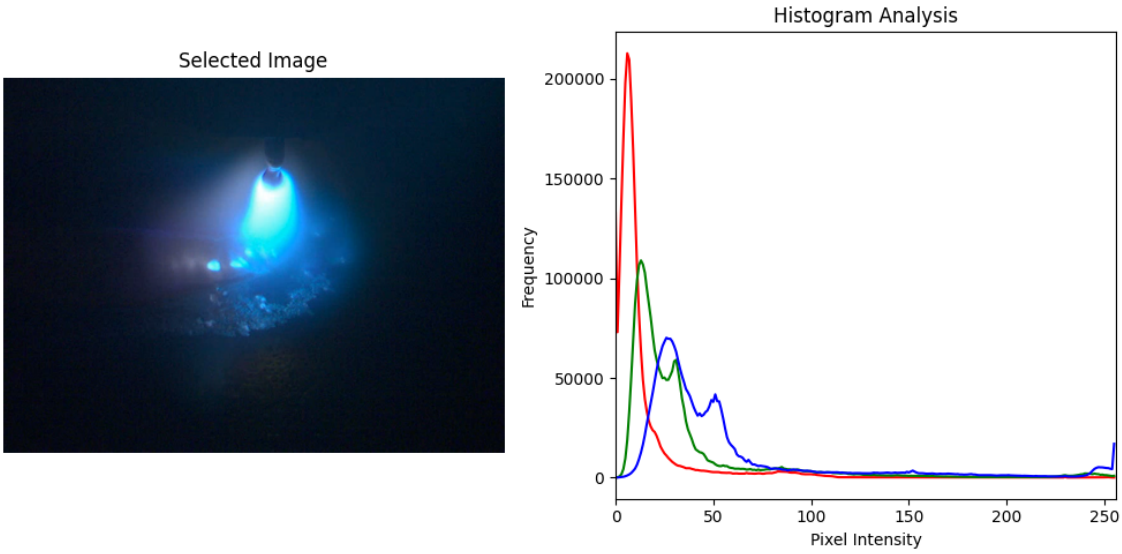
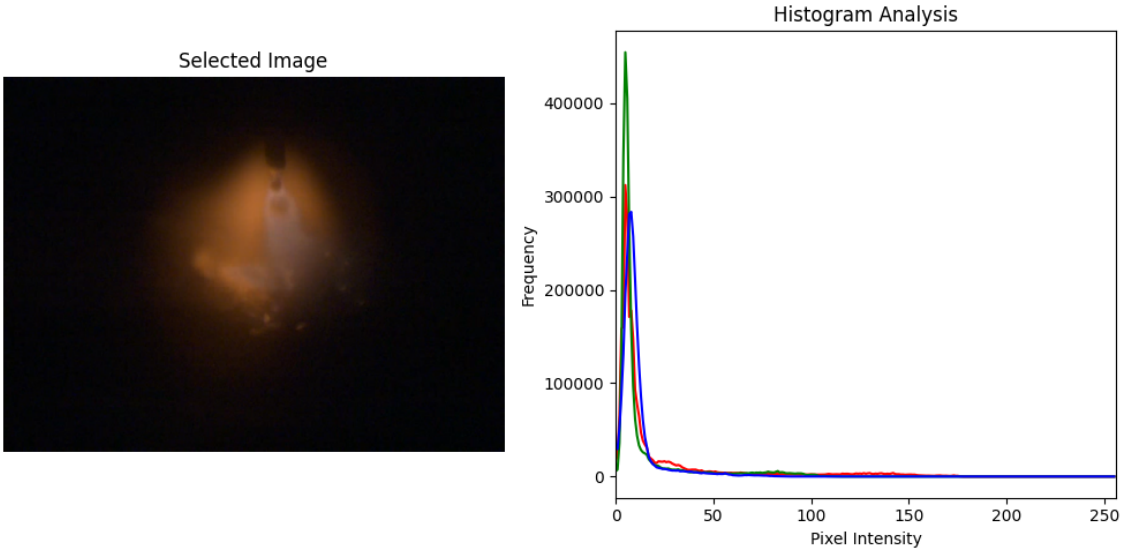


Figure 3.24: 316 LSI SS final camera setting histogram.

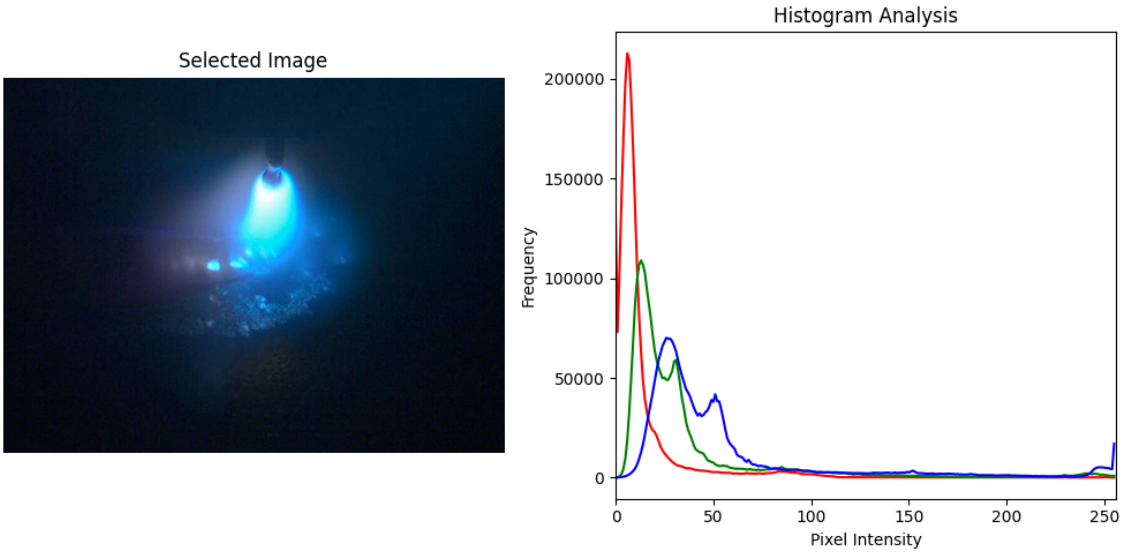


(a) 0.8 OD ND filter applied, 200μS exposure time

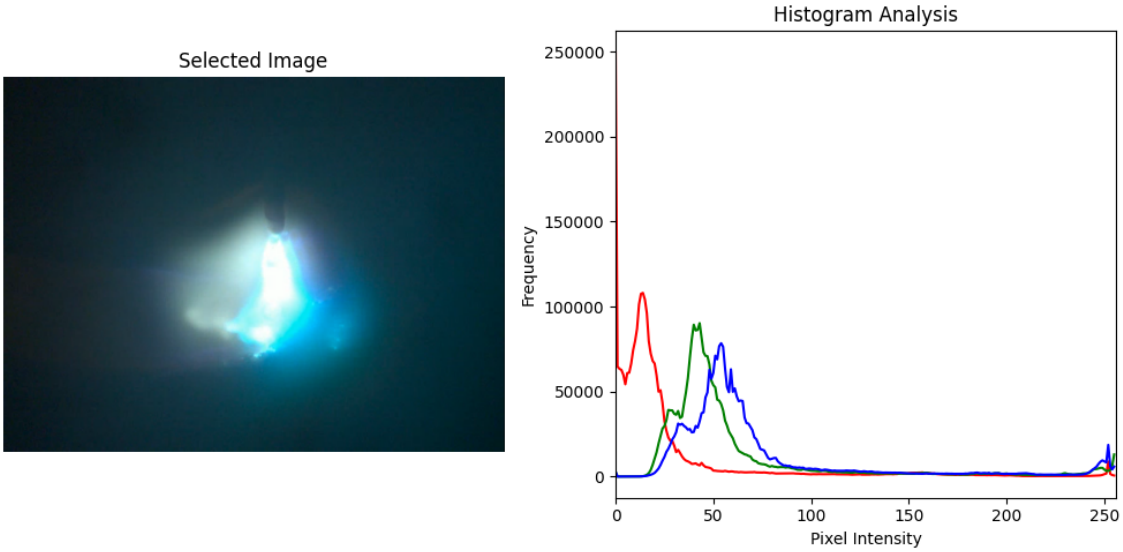


(b) 752nm bandpass filter applied, 600μS exposure time

Figure 3.25: Effect of applying 752nm bandpass filter to camera system on 410 SS WAAM deposition.



(a) 0.8 OD ND filter applied, 200μS exposure time



(b) 875nm longpass filter and 0.8 OD ND filter applied, 100μS exposure time.

Figure 3.26: Effect of applying 875nm longpass filter to camera system on 410 SS WAAM deposition.

3.4.4 Investigation of Low-Cost External Illumination

An investigation into enhancing the visibility of the deposition process by employing low-cost external illumination was conducted after the results from the ND and optical filters were obtained. The underlying hypothesis was that if an external light source of sufficient intensity could illuminate the entire deposition process, it would enable easier viewing of key deposition features. To evaluate, a Goreit G1476 [48], a low-cost LED flashlight with an advertised brightness of 20,000 lumens, was mounted to the camera sensor assembly, with its beam focused directly onto the deposition area. The deposition process was subsequently recorded using the same process in 3.4.2 with the illumination active, as depicted in Figure 3.27. However, the experimental results, shown in Figure 3.28, indicated that the arc flash remains significantly more intense than the illumination that any conventional off-the-shelf LED light source. The extreme brightness of the arc flash remained significantly more intense than the external illumination and the comparison between the results of the illuminated images and the images without it yielded no significant change in the arc flash intensity. Achieving an illumination level with LEDs sufficient to counteract the arc flash would necessitate an expensive and complex lighting system, rendering it impractical for low-cost implementations.

3.4.5 Optimal Camera Settings

The final selection for the camera settings and filter for each material can be seen in Table 3.2. The selections were selected on the basis of the clarity of the welding wire, solidification zone, and arc flash in the image.

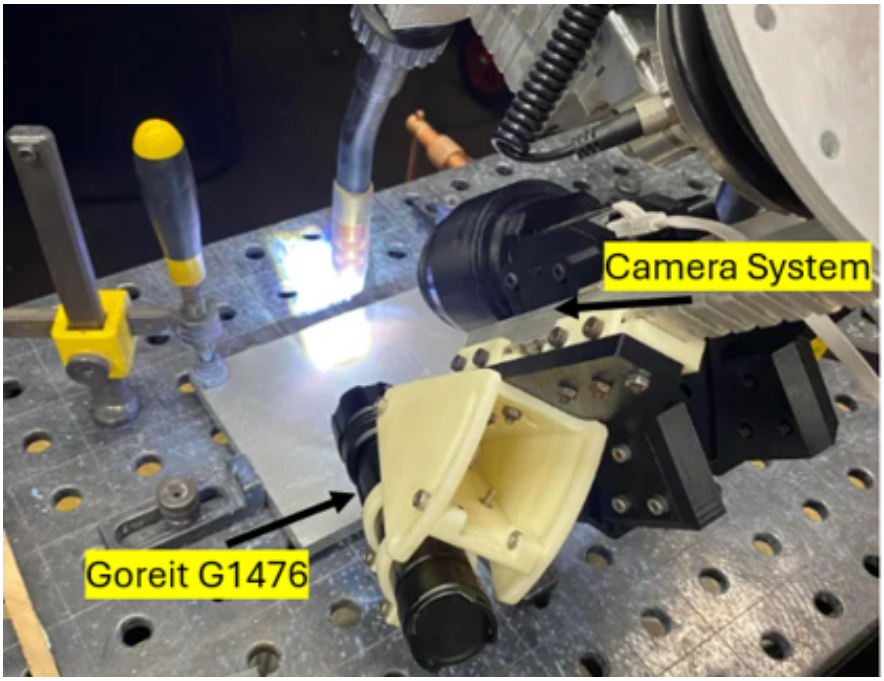
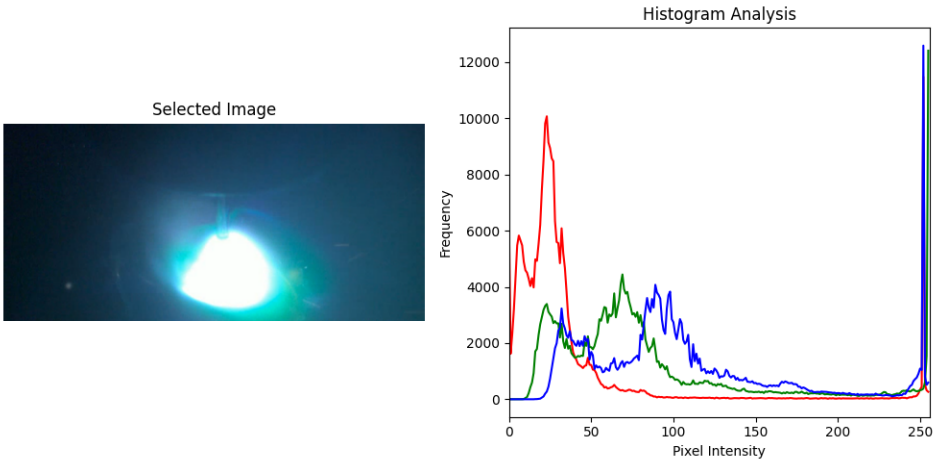


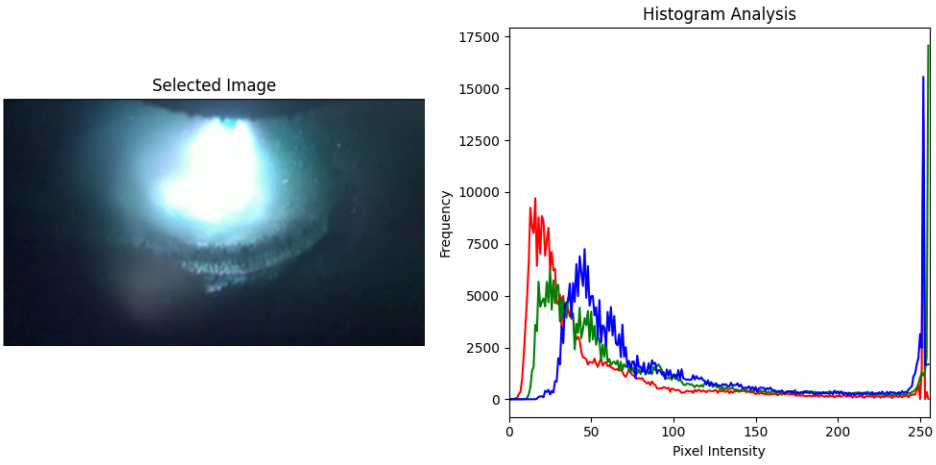
Figure 3.27: External illumination setup with camera system.

Table 3.2: Optimized Camera and Filter Settings

Material	Exposure Time μS	Filter Selection	Image
6061 RAM Al	100	1.5 OD ND	Figure 3.29c
410 SS	200	0.8 OD ND	Figure 3.29b
316 SS	1200	0.8 OD ND	Figure 3.29a

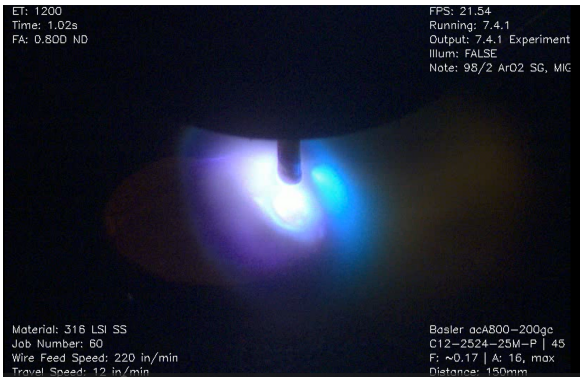


(a) No extermal illumination applied.

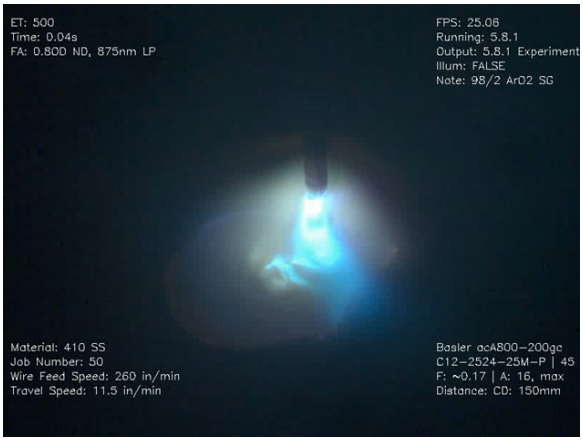


(b) External illumination applied.

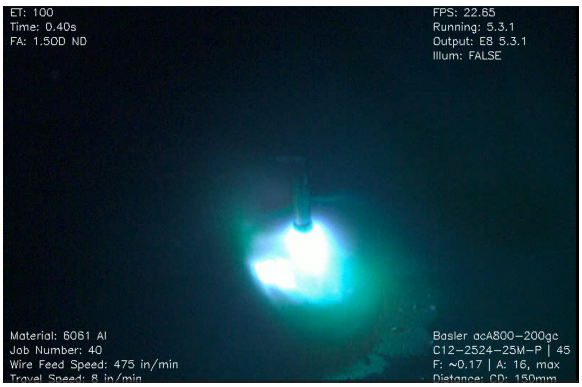
Figure 3.28: Effect of applying 20,000 lumen external illumination to 6061 Al deposition process.



(a) 316SS 1200μS exposure time, 0.8 OD ND filter



(b) 410SS 200μS exposure time, 0.8 OD ND filter



(c) 6061 RAM Al 100μS, 1.5 OD ND filter

Figure 3.29: Selected camera settings applied to ideal deposition conditions.

3.5 Image Analysis

Once images were captured and the differences between deposition settings became visually differentiable, the next phase of the study focused on image analysis. The objective was to extract and analyze pixel data from the recorded images to identify and predict deposition conditions based on observed trends within. The analysis can traditionally be done in a variety of ways, ranging from using pixel intensity values, pixel color, and overall pixel count of the objects seen in the image and comparing them. If consistent trends emerge, they can serve as predictive indicators for melt pool behavior and in-situ monitoring.

3.5.1 Pixel Segmentation

The deposition process presents challenges for standard image analysis techniques due to the complex and dynamic nature of the observed objects. The three primary objects of interest are the welding wire, the arc flash, and the solidification zone. While the arc flash is relatively easy to detect due to its high pixel intensity compared to the surrounding pixels, traditional threshold-based intensity filtering struggled with equally bright reflections on the trailing solidification zone surface, seen in Figure 3.30. Additionally, the outer edges of the arc flash vary highly in pixel intensity, making them difficult to isolate consistently.

Detecting the solidification zone and welding wire is even more challenging. Their size fluctuates with the heat input and their brightness, as seen by the camera, varies depending on their proximity to the arc flash. As these objects move closer to the high-intensity region created by the arc flash, they become significantly brighter, leading to inconsistent intensity-based detection. Furthermore, the solidification zone exhibits significant color variation due to the metal's phase changes and its proximity to the arc flash, complicating traditional classification methods.

Due to these limitations, a more advanced classification and segmentation approach was required to accurately extract the object pixel data from the images to build correlations between them and changes in deposition.

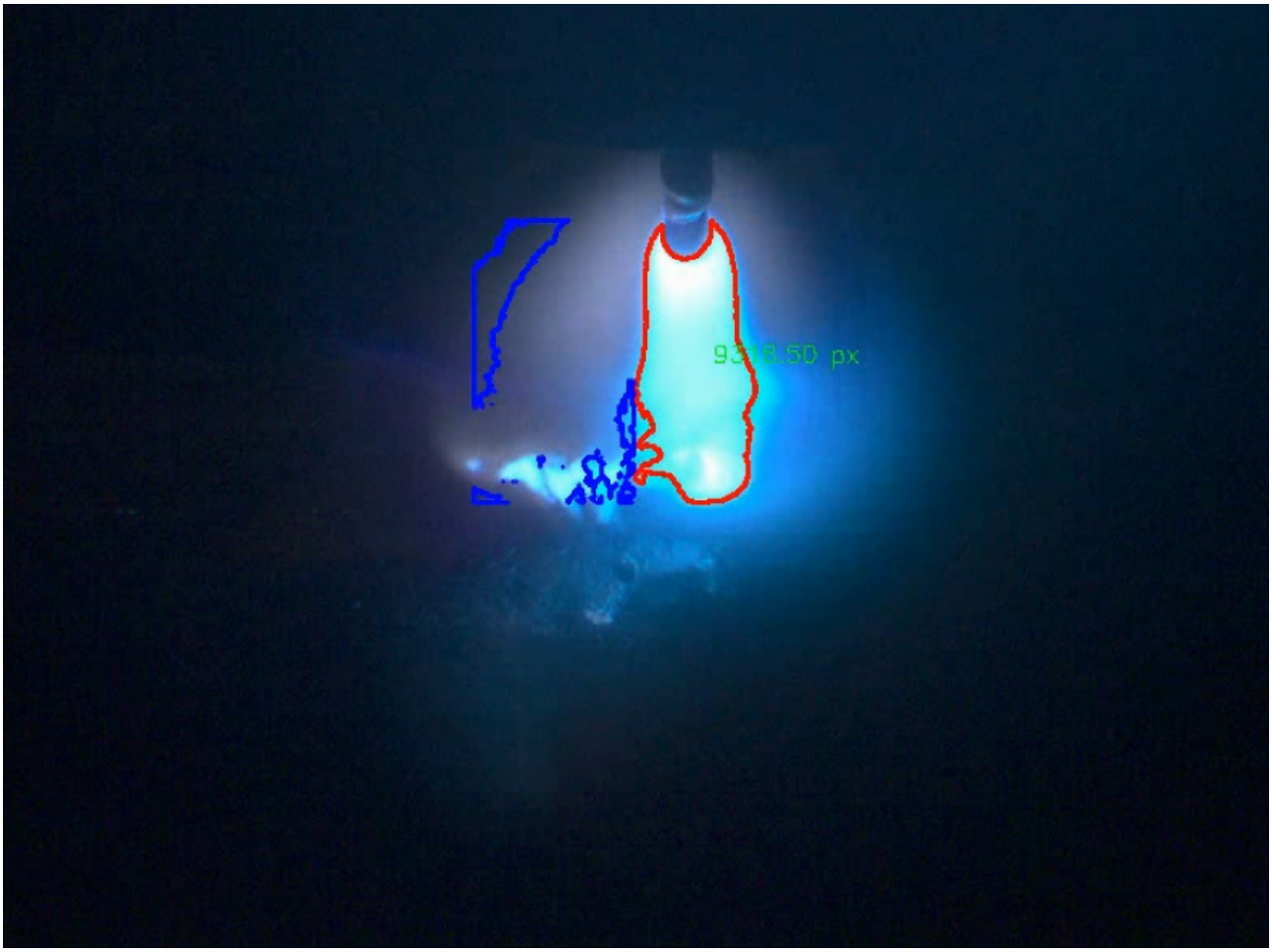


Figure 3.30: Threshold pixel analysis on WAAM deposition.

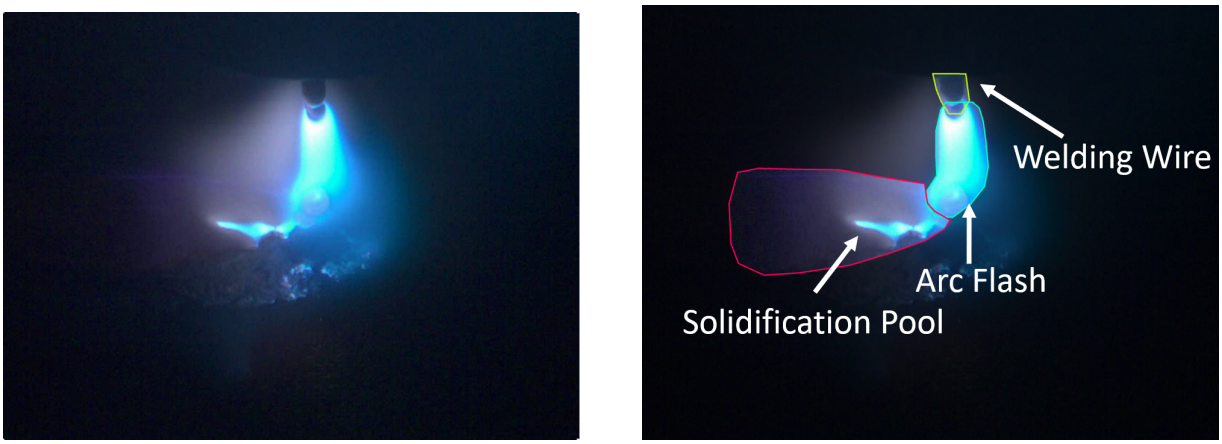
3.5.2 Machine Learning Based Segmentation

With recent advances in machine learning (ML) capabilities, problems such as isolating and detecting objects in these images is a perfect application. The detection algorithm selected for this research was YOLOv8 [49] because of its ease of use, open-source literature, and proven use in previous WAAM research [50]. It is a ML approach using a neural network that classifies each pixel based on predefined object classes set by the user.

To have a sufficient machine learning model, high-quality labeled data must be constructed. Image frames from every type of experiment were extracted with 15 to 30 frames being used per trial, depending on the length of the video and image data available. Each frame was manually outlined using Roboflow [51]. The resulting data consisted of an image and an accompanying .txt file. The file contained information on the three classes, including the pixel coordinates of each class's center and details about the size of the outline. An example of what outlining is seen in Figure 3.31. The data was then imported into a Python script that trained a YOLOv8 model on the images, with 60% being used for training, 20% being used for validation, and 20% being used to test the results. The model was trained on 50 iterations of 284 total images.

The resulting images contained an outline segmentation of any class seen by the model and information about the outline's height, width, total pixel count/area, and the maximum and minimum coordinate values within an X,Y Cartesian coordinate frame. An example is seen in Figure 3.32. The data was then used to compare the area of the segmentation and average location in each frame to the changes made to the deposition process in the experiment to observe trends.

Pixel measurement data was used in place of physical measurements of the deposition objects because of the need for calibration of the image to compensate for the monitoring angle, and the multiple angles needed to measure object size when viewing three dimensional objects that can vary in distance from the camera lens, such as the edges of the solidification zone [52, 19].



(a) Sample deposition image. **(b)** Manual object class outlining.

Figure 3.31: Object class outlining procedure.



(a) Raw WAAM deposition image. **(b)** Image segmentation algorithm applied.

Figure 3.32: Object class outlining procedure.

3.6 Process Changes, Defects, and Part Monitoring

3.6.1 Deposition Parameter Variations

With the camera settings and filters selected, the next phase of the study focused on introducing deposition defects and process variations to analyze their visual characteristics and establish any diagnostic criteria based on the recorded footage. Introducing these changes in a controlled manner allows for direct comparison between the video feed and the predefined defected characteristics, allowing for a systematic evaluation between the two.

The first test of changing deposition conditions was done by changing the wire feed speed of the material being deposited. The theory being verified is that the varying wire feed speed of the deposition would result in a lower deposition rate and, therefore, a lower heat input of the deposition. Such a change would theoretically result in differences in the deposition images visible to the camera, making them detectable in post-process analysis.

To test, a set of experiments was developed to first implement the selected camera settings and filters as seen in Table 3.2 and then test changes in wire feed speed while keeping the travel speed of the robot the same, ensuring a change in heat input. The change in wire feed speed was based on the optimal deposition parameters established in Table 3.1, and can be seen in Table 3.3 and Table 3.4. The deposition parameters were established to encompass heat input rates that were significantly below optimal and significantly higher than optimal, resulting in images that could be used to observe both conditions.

Table 3.3: Deposition settings for heat input testing, 410 SS material, 6.35 mm/s travel speed.

Current (A)	Voltage (V)	WFS (mm/s)	HI (J/mm)
126	19.4	67.7	308
134	19.8	72.0	334.3
141	20	76.2	355.3
145	20.2	80.4	369
148	20.3	84.7	378.5
154	20.6	88.9	399.7
162	20.9	93.1	426.6
170	21.3	97.4	456.2

Table 3.4: Deposition settings for heat input testing, 316 LSI SS material, 5.08 mm/s travel speed.

Current (A)	Voltage (V)	WFS (mm/s)	HI (J/mm)
150	12.7	72	300
155	12.9	76.2	314.9
160	13	80.4	327.6
166	13.2	84.7	345.1
171	13.4	88.9	360.9
178	14.3	93.1	400.9
185	15.1	97.4	439.9
192	15.9	101.6	480.8
199	16.7	105.8	523.4

3.6.2 Deposition Defect Introduction

The second change in the deposition conditions was the intentional introduction of defects by removing the shielding gas, depositing material on unprepared, dirty substrates, and significantly lowering the heat input of the process. Shielding gas is critical for preventing oxidation contamination and for providing a cooling effect to the solidification process. Removing it can lead to porosity and inconsistent arc stability. In addition, deposition of material on a contaminated or improperly prepared substrate-particularly in aluminum-increases defect formation. Table 3.5 is a summary of the settings used for this experiment, with the changes being compared to the ideal deposition settings seen in Table 3.1.

3.6.3 Constant Heat Input With Varying Deposition Parameters

The third condition tested was the viewing of deposits with a constant heat input but varying deposition parameters. Since the formula for heat input, seen in Equation 3.2, is a fractional equation containing both power and travel speed, changing either quantity in a proportional amount results in the same heat input being applied to the deposition. The theory being tested is that if there is any variation in the deposition dynamics within the same heat input, then they might be visible in the deposition video and therefore detectable in-situ.

To test, material depositions were conducted with the parameters seen in Table 3.6 and the optimal camera settings in Table 3.2

3.6.4 Part Monitoring

The final experiment conducted was to investigate the camera setup's ability to monitor melt pool behavior during a WAAM build. To do this, a simple part build was conducted with alternating build directions (y and -y) on each layer with the camera settings defined in Table 3.2. The material used was 316 LSI SS with the weld settings seen in Table 3.1. Before each layer was deposited, the part was allowed to cool to 120°C to maintain a constant interpass temperature between layers. The part was constructed with 21 total deposition layers and was roughly 122mm in length by 10mm in width by 56mm in height.

Table 3.5: Deposition defect parameters used to observe differences in defective depositions compared to optimal settings seen in table 3.1.

Material	Shielding Gas	HI (J/mm)	Substrate
6061 RAM Al	100% Ar	706.0	Prepared
6061 RAM Al	None	186.7	Unprepared
410 SS	98% Ar, 2% O_2	399.7	Prepared
410 SS	None	399.7	Prepared

Table 3.6: Constant heat input parameters for 316 LSI SS material. Used to observe differences in deposition images with changing wire feed speed and travel speed while maintaining heat input of 360 J/mm.

Current (A)	Voltage (V)	WFS (mm/s)	TS (mm/s)
155	12.9	76.2	4.4
160	13	80.4	4.6
166	13.2	84.7	4.8
171	13.4	88.9	5.1
178	14.3	93.1	5.6

Chapter 4

Results and Discussion

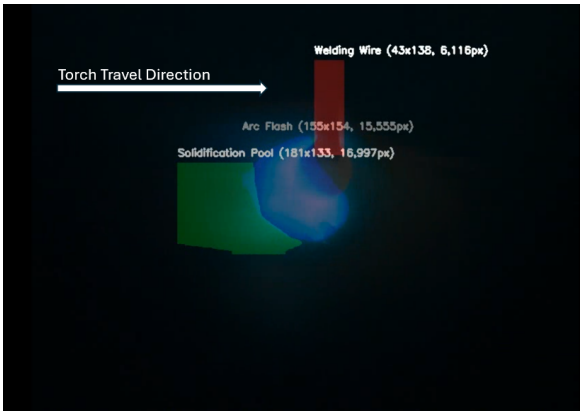
4.1 Correlation Between Heat Input, Solidification Zone Size, and Wire Area.

The results of material deposition at both lower and higher than normal wire feed speeds revealed significant changes in key visual features of the process. These changes included variations in the pixel area of the solidification zone, the amount of welding wire visible, and changes in the arc length.

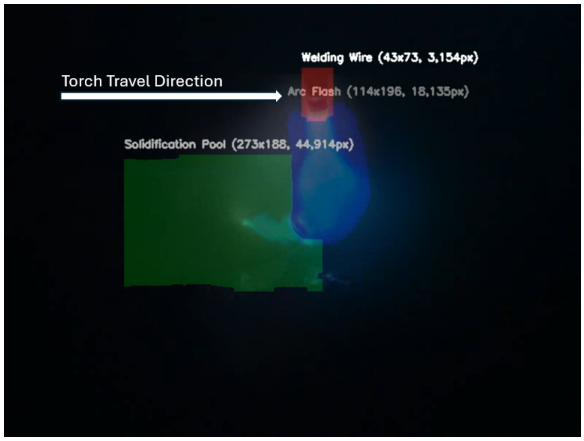
At lower wire feed speeds, both voltage and current decreased, leading to a reduction in arc intensity and increase in the amount of welding wire visible from the smaller arc associated with a drop in voltage. Additionally, the visible solidification zone decreased in length and width due to the reduced material deposition from the lower current.

Conversely, at higher wire feed speeds, both voltage and current increased, causing the arc length to expand. The increase in arc length led to less visible welding wire in the images and an increase in arc intensity, as the higher voltage extended the arc. The visible solidification zone also grew in length and width, reflecting the increased amount of material being melted due to the higher current during deposition. These changes can be observed in Figure 4.1 and Figure 4.2.

A summary of these findings is provided in Table 4.1.

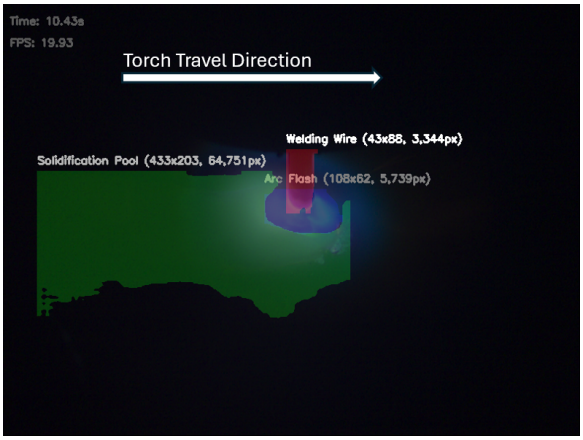


(a) 410SS 67.7mm/s WFS.

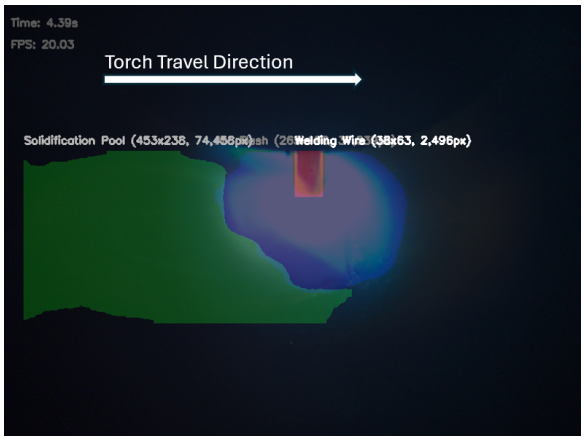


(b) 410SS 97.3mm/s WFS

Figure 4.1: Effect of increasing the wire feed speed on the images seen by the camera system on 410SS WAAM deposition.



(a) 316SS 67.7mm/s WFS.



(b) 316SS 105.8mm/s WFS.

Figure 4.2: Effect of increasing the wire feed speed on the images seen by the camera system on 316SS WAAM deposition.

Table 4.1: Four test conditions from 4.1 of variable wire feed speed settings tested with a 0.8 OD ND filter applied.

Material	Exposure Time (μS)	WFS (mm/s)	Image
410 SS	200	67.7	Figure 4.1a
410 SS	200	97.3	Figure 4.1b
316 SS	1200	67.7	Figure 4.2a
316 SS	1200	105.8	Figure 4.2b

The YOLOv8 image segmentation model was then applied to the resultant deposition images, and the segmentation data was collected and graphed versus the heat input from the wire feed speed variation, seen in Figure 4.3 and Figure 4.4. Analysis of the graphs reveals a strong positive correlation between heat input and the average solidification zone area for both materials. A weaker negative correlation is observed with the average welding wire area, while the arc flash remains inconclusive. However, this trend is expected, as a higher heat input increases the amount of wleding wire being melted, resulting in greater material deposition. Additionally, the elevated temperature of the part from the increasing heat input extends the solidification time of the material after it is deposited, leading to a larger solidification zone. These findings strongly suggest that this camera system provides an effective method for monitoring melt pool heat input variations seen through the camera feed during the deposition process.

4.2 Deposition Defect Correlation

Introducing defects into the deposition process also produced visual changes and changes in resultant segmentation data. Turning off the shielding gas, introducing substrate contamination, and lowering the wire feed speed the wire feed speed by 65% (in the case of 6061 Al) resulted in erratic and inconsistent material depositions. The arc flash area exhibited significant variability, and the solidification zone became much more turbulent, changing the observed size of the object feature in the video feed. Additionally, spatter increased substantially, with larger molten droplets dispersing randomly in every direction from the melt pool, seen in Figure 4.5. Examples of the images with the defects described in 3.5 are seen in Figure 4.6, showing turbulence in the melt pool.

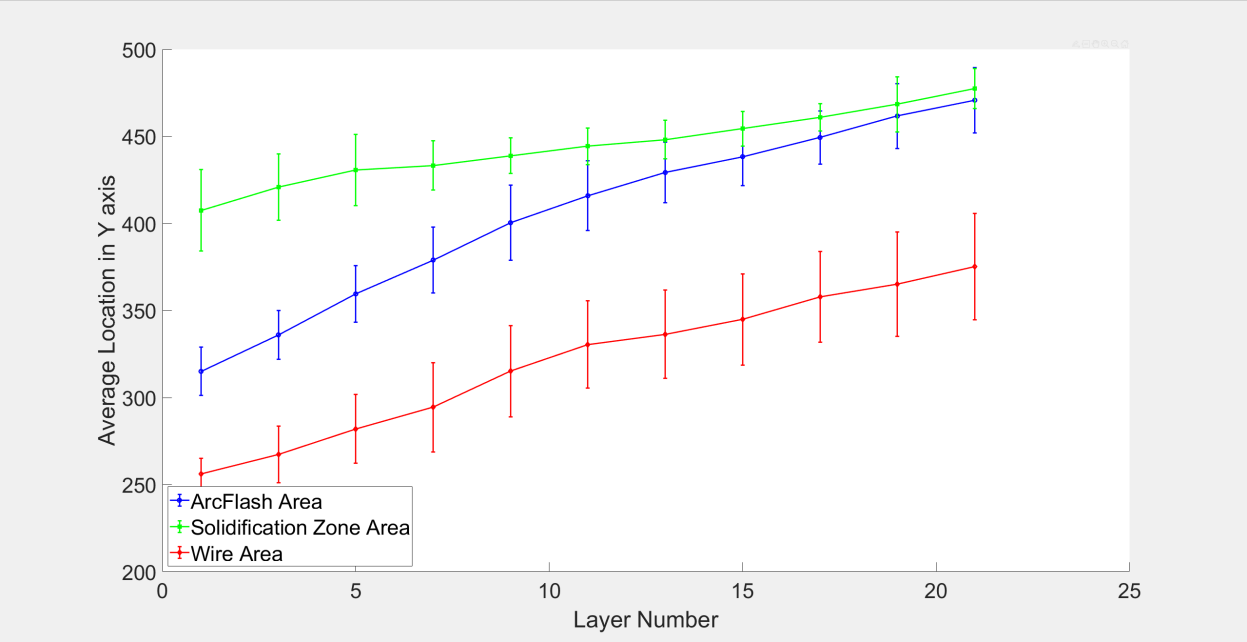


Figure 4.3: Evident solidification zone and welding wire pixel area trends with changes in heat input for 316 LSI SS material.

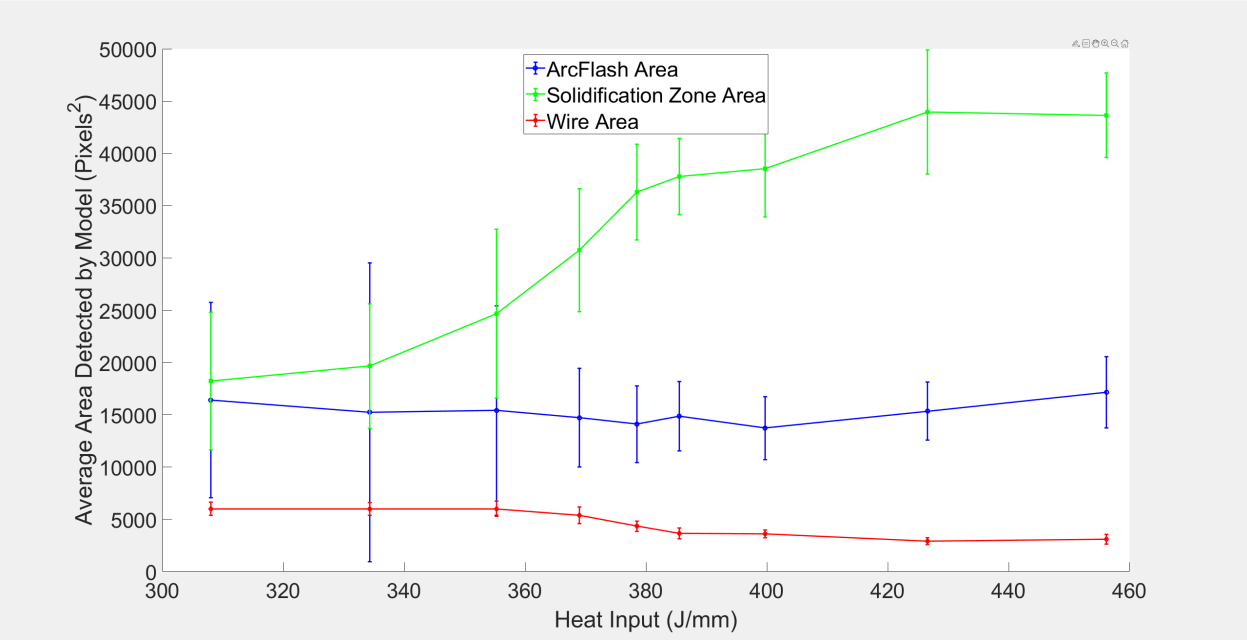


Figure 4.4: Evident solidification zone and welding wire pixel area trends with changes in heat input for 410SS material.

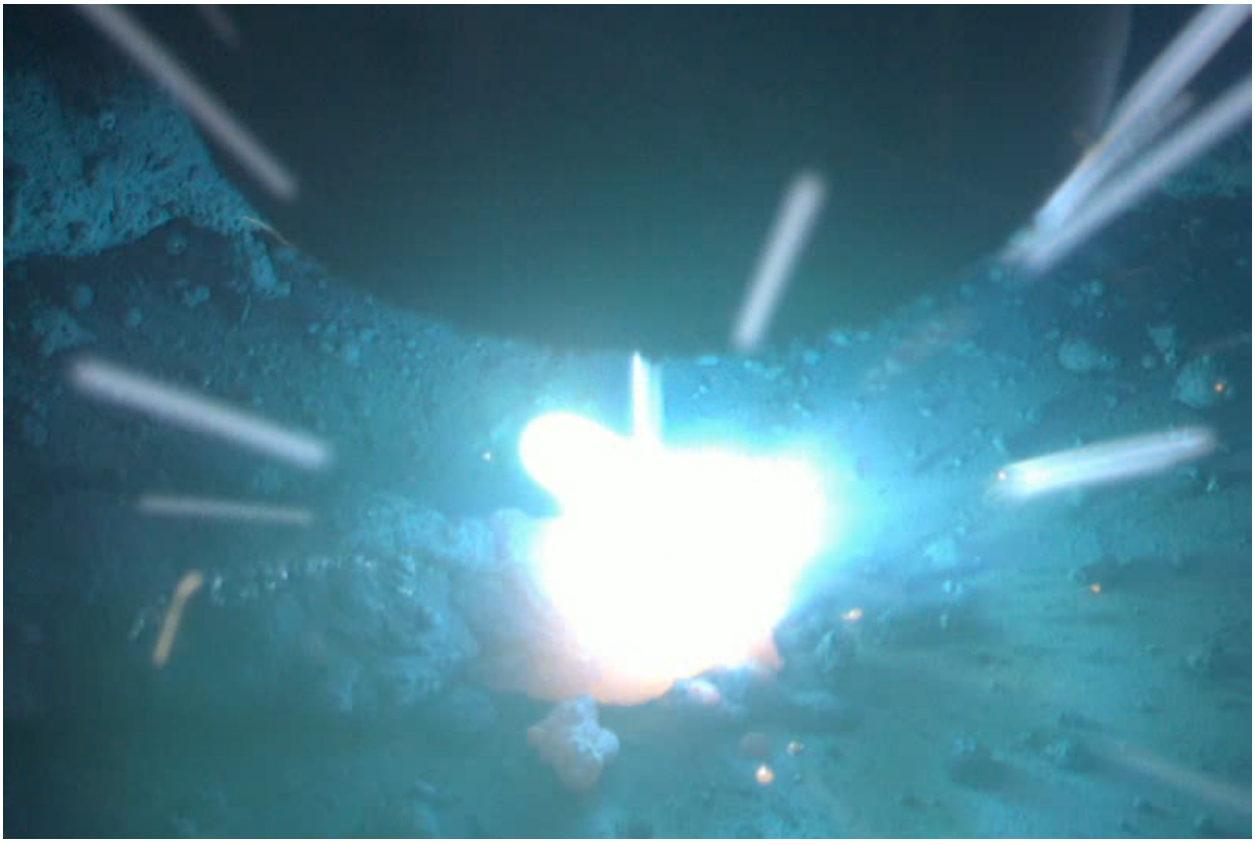
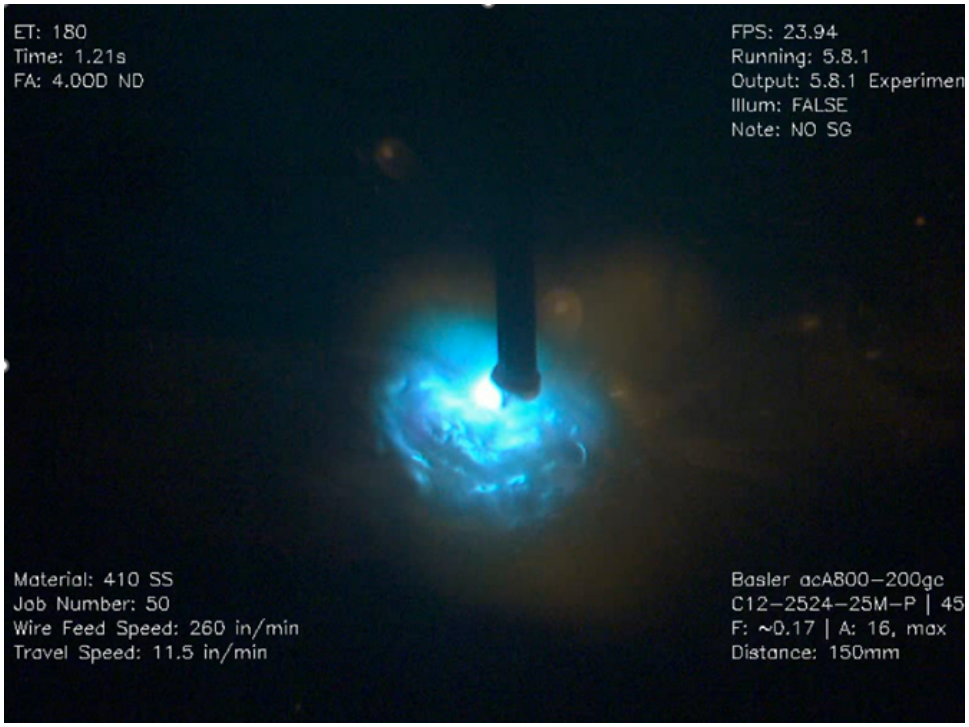
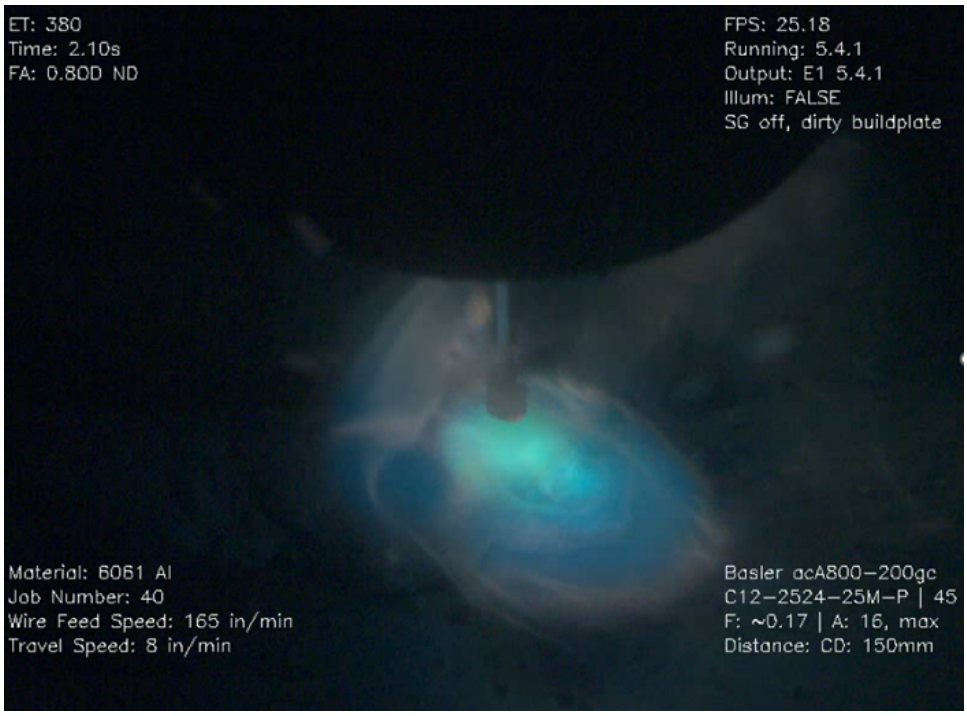


Figure 4.5: Large spatter streaks visible in video feed.



(a) 410SS deposition with no shielding gas.



(b) 6061 aluminum deposition with no shielding gas and a low heat input.

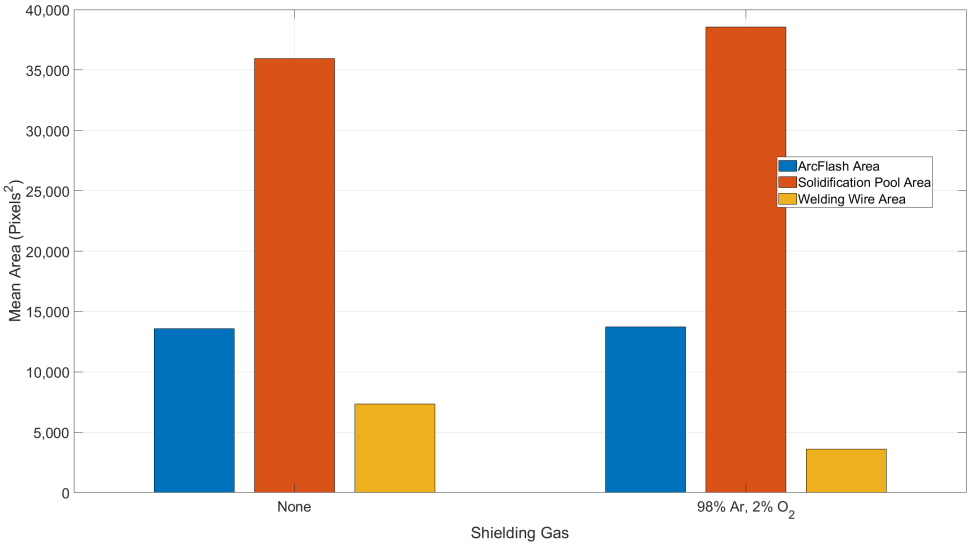
Figure 4.6: Erratic behavior seen in deposition defect conditions.

The application of the YOLOv8 image segmentation model illustrates the effects of introducing the respective deposition defects. For aluminum, the pixel area detected for each feature is significantly smaller compared to the experiment with optimal deposition settings. However, this reduction is not solely due to the removal of shielding gas and the use of an unprepared substrate; it is also partially influenced by the lower wire feed speed used in this experiment. A more reliable indicator of the erratic behavior introduced by these defects is the standard deviation of the detected feature. While the standard deviation of the solidification zone pixel area remains relatively constant, the erratic behavior of the arc flash contributes to a rise in its standard deviation. Figure 4.8

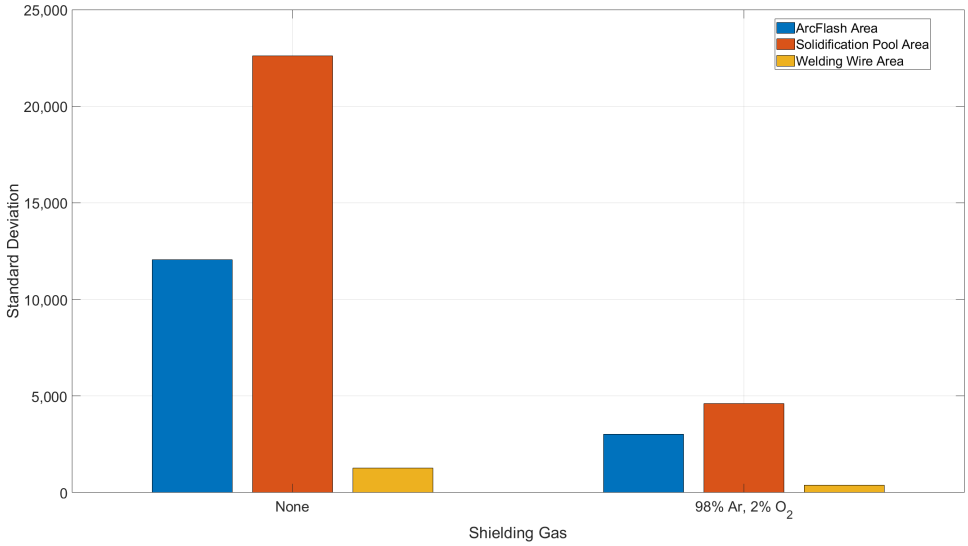
The application of the model on the 410SS revealed significant differences of the standard deviation for all features and pixel area of the solidification zone detected by the model, as seen in Figure 4.7. Since this test was performed with the same deposition settings with the only change being the removal of the shielding gas, these changes can be directly attributed to it. The increased standard deviation reflects greater instability in the deposition, likely due to the increased oxidation and lack of cooling from the absence of the shielding gas.

4.3 Deposition Images with Same Heat Input

When varying the wire feed speed and travel speed while maintaining a constant heat input, it was expected that the resulting deposition would exhibit negligible differences. The model's analysis largely supports this hypothesis, as the detected average areas of arc flash and welding wire remain nearly unchanged, as shown in Figure 4.9. However, a slight correlation is observed between the arc flash area and increased wire feed speed and decreased travel speed, suggesting a minor deviation in the detected features. The arc flash could be larger as the wire feed speed increases, but it is also possible that the result is due to errors in the model's analysis. Potential sources of error include variations in arc stability or the model's ability to accurately differentiate overlapping regions.

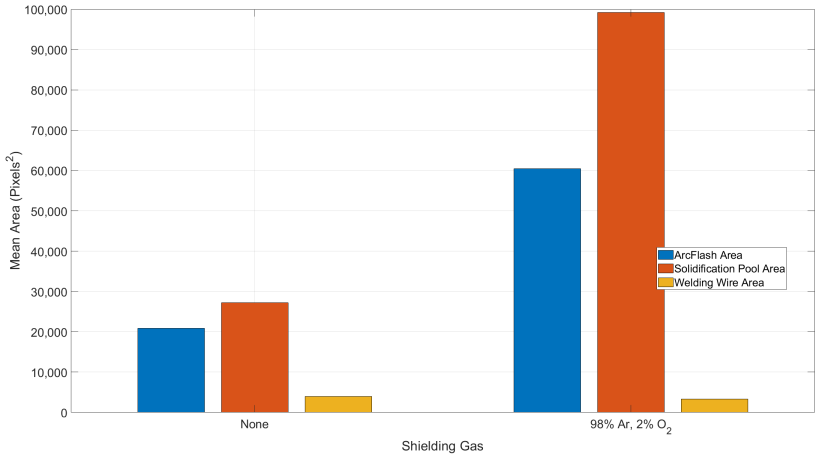


(a) 410 SS average of feature area detected.

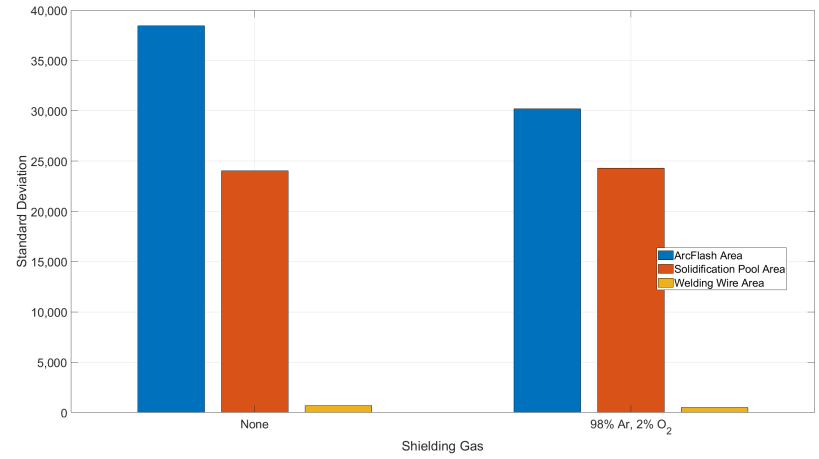


(b) 410 SS standard deviation of feature area detected.

Figure 4.7: Effect on pixel area with shielding gas removed for 410 SS. slightly different feature area, much higher standard deviation.



(a) 6061 Al average of feature area detected.



(b) 6061 Al standard deviation of feature area detected by model.

Figure 4.8: Effect on pixel area seen by model with shielding gas removed and lower heat input for 6061 RAM Al. Much smaller feature area detected with change in standard deviation for arc flash area.

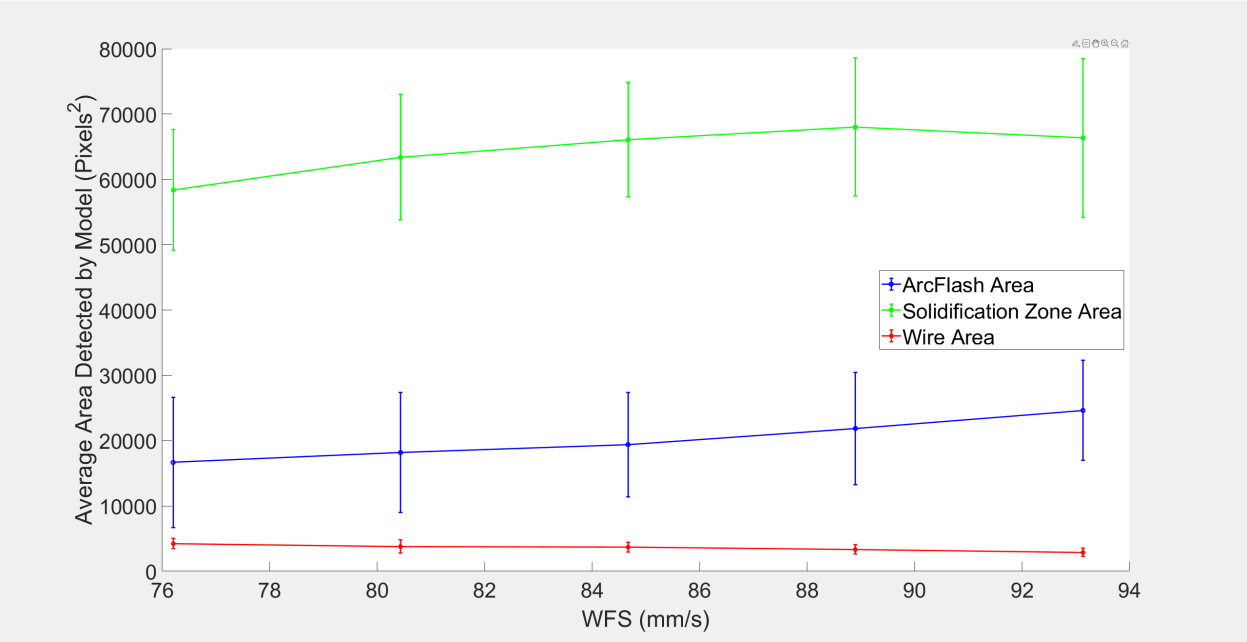
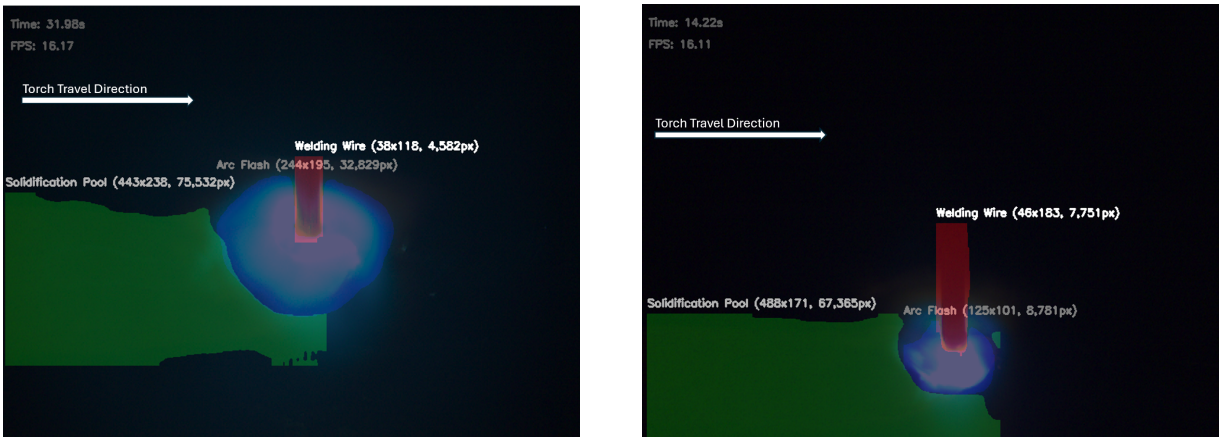


Figure 4.9: No clear change in pixel area detected by model with constant heat input settings.

4.4 Demonstration of WAAM Part Monitoring

The part monitoring experiment was the most critical assessment conducted to evaluate the effectiveness of this monitoring system, as it closely simulates a real-world application. If the system demonstrates reliable performance in this setting for detecting process changes, it could have further practical implementation in a production environment. The final part, a wall, consisted of 21 layers and is shown in Figure 4.11 and the deposition images from the monitoring system on layers 2 and 20 can be seen in Figure 4.10, respectively. The initial path plan was made on the assumption that each deposition bead was 3 mm in height. However, this value serves as a rough approximation. Deposition bead height is influenced by several factors including the cooling effects of underlying layers, melt pool behavior, arc dynamics, and the overall temperature of the build. As a result, as the structure accumulates layers, variations in the deposition bead height occur, often being shorter than expected. The effect compounds in each layer, progressively increasing the distance from the contact tip to the workpiece (CTWD) and eventually leading to inadequate shielding gas coverage and incorrect prediction of the start of the next deposition bead during path planning, which causes process defects that impact the quality of the final part.

Given the common increase in CTWD during part builds, the ability to detect and monitor this change is crucial for determining when it begins to impact deposition quality. Detecting the CTWD change is done by correlating the position of the feature detected by the model in an X,Y Cartesian plane to the CTWD on the first deposition. If the parameters of the deposition remain constant for each layer, then the changing position of the feature as seen in the image feed and/or an increase in the amount of welding wire seen indicates the CTWD is changing. Image analysis from the experiment reveals a strong correlation between the detected feature positions and the layer number, indicating that the system effectively tracks changes in the contact tip to workpiece distance as the build progresses. The trend is visualized in Figure 4.10.



(a) Layer 2 part monitoring segmentation.

(b) Layer 20 part monitoring segmentation.

Figure 4.10: Change in location of deposition location in camera system feed after 18 layers of deposition.

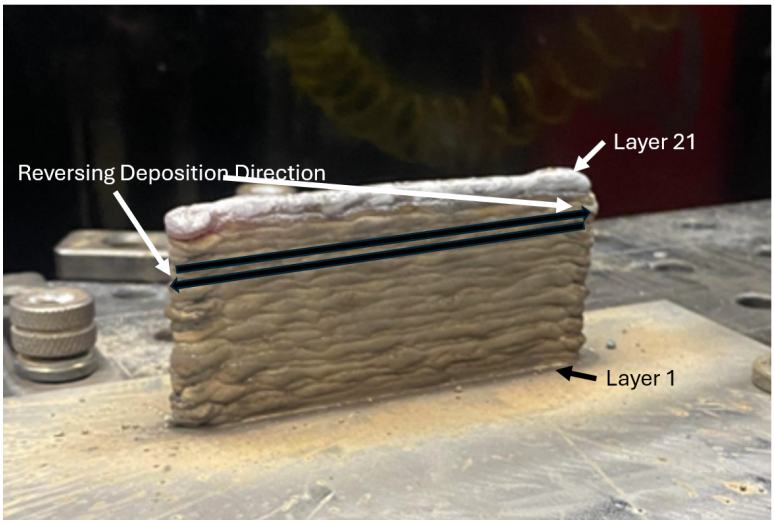


Figure 4.11: 316 LSI part from part monitoring experiment.

However, the feature detection accuracy is affected by the alternating deposition direction used in the part build process. With each successive layer, the deposition path reverses, causing the solidification zone's position to reverse accordingly. The directional change introduces variability in the detected features, as seen in the data, where each layer switch results in a sharp change in solidification zone area, forming a sawtooth pattern. The inconsistency is likely due to the model being trained on only 20% of the data in the positive y direction, which limits its accuracy in those cases. To address this issue in future studies, mirroring the images collected during deposition in the positive y-direction or mirroring the entire dataset for all experiments would be a viable solution.

After removing the layers deposited in the positive y global coordinate build direction, a consistent positive trend emerged between the detected welding wire feature location along the y-axis in the monitoring system's image and the layer number (see Figure 4.12). The trend is significant because it directly reflects changes in the CTWD, as the deposition parameters remain consistent across layers. The results indicate that the deposition height is less than the assumed 3mm, meaning that further depositions will require adjustments in the path planning to compensate for the smaller than planned part or further WAAM part build development for more consistent deposition bead height.

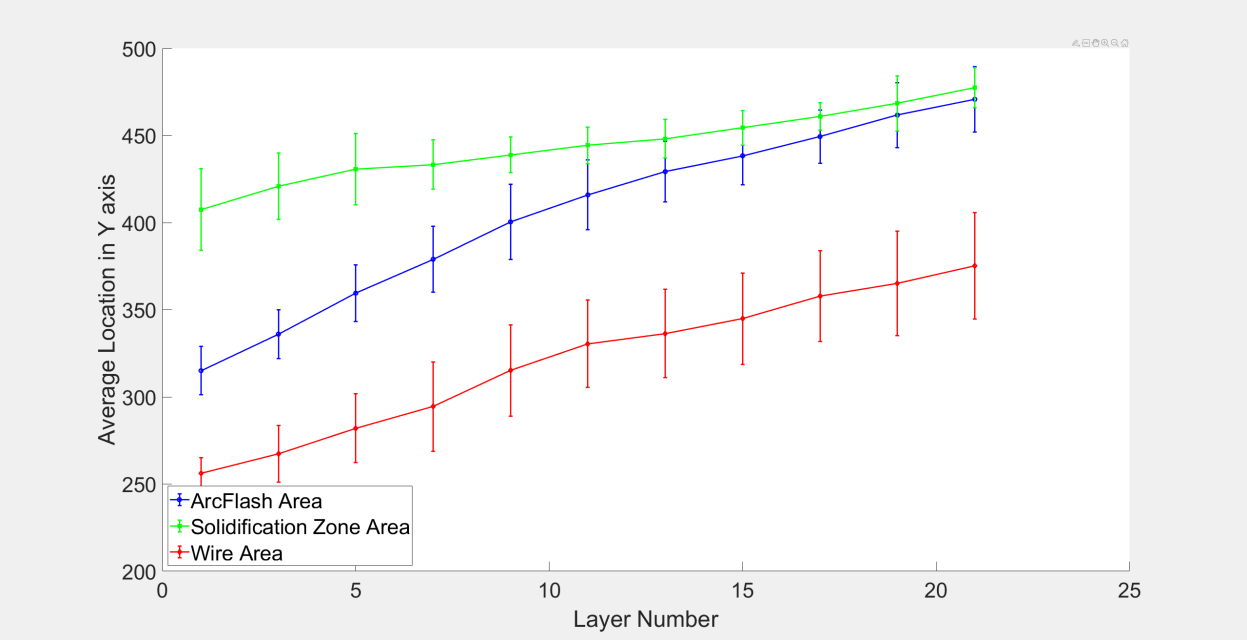


Figure 4.12: Part build in positive Y direction showing strong trend in location change versus layer number.

Chapter 5

Conclusions and Recommendations

In conclusion, WAAM is an emerging technology that has great potential in building large-scale components with significantly improved efficiency. However, maintaining consistent part quality without defects remains a challenge. Monitoring the deposition process for stability or to detect defects is a necessary component for employing this manufacturing method. The research conducted explored a method of low-cost monitoring to accomplish this goal, with a low-cost camera, lens, neutral density filter selection, and readily available software being employed. The method to monitor the deposition process started with establishing a camera mount for viewing the deposition features at a repeatable angle and distance, then selecting camera settings and filter selections for best mitigating the arc flash. A method for analyzing the image feed was then established by training and employing an open source image segmentation ML model. Various deposition conditions, including the introduction of defects, and a sample part build were viewed and analyzed with the model to observe trends between the conditions and the deposition features seen in the image feed. The results showed promising trends among heat input and feature size in the image, standard deviation changes for deposition conditions absent of shielding gas, and changes in centroid location for the features in a part build as the CTWD increased.

In order for large scale adoption of the established low-cost monitoring method, additional research is needed. Establishing a way to monitor the deposition process in-situ to alert the operator if defects occur will require further training of the dataset on additional defects and materials common in the WAAM manufacturing of a part. In addition, the speed of

the model's analysis must be increased, as the current YOLOv8 image segmentation is a relatively slow process, with each frame taking roughly 60-80ms to analyze, resulting in a maximum fps of around 12-16 if employed in-situ as is. Addressing both challenges will involve employing a faster ML model or optimizing the current one, with additional training for defects and on other materials required in either case.

Bibliography

[1] Sue Roberts. Wire-arc additive manufacturing can be used to build very large parts to near-net shape, April 2020. URL https://www.thefabricator.com/additivereport/article/additive/wire-arc-additive-manufacturing-can-be-used-to-build-very-large-parts-to-near-net-shape. viii, 2

[2] Monitor and computer tower vector image on VectorStock, . URL https://www.vectorstock.com/royalty-free-vector/monitor-and-computer-tower-vector-2754008. viii, 12

[3] Picatinny Rails, . URL https://grovtec.com/collections/picatinny-rails. viii, 11, 14

[4] ace acA800-200gc | GigE Camera | Basler | Basler AG, . URL https://www.baslerweb.com/en-us/shop/aca800-200gc/. viii, 17, 21

[5] Z. Zeng, B. Q Cong, J. P. Oliveira, W. C Ke, N. Schell, B. Peng, Z. W. Qi, F. G Ge, W. Zhang, and S. S. Ao. Wire and arc additive manufacturing of a Ni-rich NiTi shape memory alloy: Microstructure and mechanical properties. *Additive Manufacturing*, 32: 101051, March 2020. ISSN 2214-8604. doi: 10.1016/j.addma.2020.101051. URL https://www.sciencedirect.com/science/article/pii/S2214860419315672. 1

[6] Tiago A. Rodrigues, N. Bairrão, Francisco Werley Cipriano Farias, A. Shamsolhodaei, Jiajia Shen, N. Zhou, Emad Maawad, Norbert Schell, Telmo G. Santos, and J. P. Oliveira. Steel-copper functionally graded material produced by twin-wire and arc additive manufacturing (T-WAAM). *Materials & Design*, 213:110270, January 2022. ISSN 0264-1275. doi: 10.1016/j.matdes.2021.110270. URL https://www.sciencedirect.com/science/article/pii/S026412752100825X. 1, 3

[7] Wei Ya and Kelvin Hamilton. On-Demand Spare Parts for the Marine Industry with Directed Energy Deposition: Propeller Use Case. In *Industrializing Additive Manufacturing: Proceedings of Additive Manufacturing in Products and Applications - AMPA2017*, pages 70–81. Springer, September 2017. doi: 10.1007/978-3-319-66866-6_7. URL https://research.utwente.nl/en/publications/on-demand-spare-parts-for-the-marine-industry-with-directed-energ. 3

[8] S. W. Williams, F. Martina, A. C. Addison, J. Ding, G. Pardal, and P. Colegrove. Wire + Arc Additive Manufacturing. *Materials Science and Technology*, 32(7):641–647, May 2016. ISSN 0267-0836. doi: 10.1179/1743284715Y.0000000073. URL https://doi.org/10.1179/1743284715Y.0000000073. Publisher: SAGE Publications. 3

[9] Jigar Shah, Gaurav Patel, and Jatin Makwana. Optimization and Prediction Of MIG Welding Process Parameters Using ANN. *INTERNATIONAL JOURNAL OF ENGINEERING DEVELOPMENT AND RESEARCH*, 5(2):1487–1492, May 2017. ISSN 2321-9939. URL https://rjwave.org/ijedr/viewpaperforall.php?paper=IJEDR1702233. Publisher: IJEDR (www.ijedr.org). 3

[10] Ajit Hooda, Ashwani Dhingra, and Satpal Sharma. OPTIMIZATION OF MIG WELDING PROCESS PARAMETERS TO PREDICT MAXIMUM YIELD STRENGTH IN AISI 1040. 2012. 3

[11] K. R. Madavi, B. F. Jogi, and G. S. Lohar. Metal inert gas (MIG) welding process: A study of effect of welding parameters. *Materials Today: Proceedings*, 51:690–698, January 2022. ISSN 2214-7853. doi: 10.1016/j.matpr.2021.06.206. URL https://www.sciencedirect.com/science/article/pii/S2214785321045776. 3

[12] Akshat Sharma, Ayush Verma, Devashish Vashisth, and Pradeep Khanna. Prediction of bead geometry parameters in MIG welded aluminium alloy 8011 plates. *Materials Today: Proceedings*, 62:2787–2793, January 2022. ISSN 2214-7853. doi: 10.1016/j.matpr.2022.02.063. URL https://www.sciencedirect.com/science/article/pii/S2214785322006356. 3

[13] Piotr. What Are Stickout, Electrode Extension and Contact-Tip-To-Work Distance?, March 2021. URL https://elgawelding.com/what-are-stickout-electrode-extension-and-contact-tip-to-work-distance/. 4

[14] Xi Chen, Fanrong Kong, Youheng Fu, Xushan Zhao, Runsheng Li, Guilan Wang, and Haiou Zhang. A review on wire-arc additive manufacturing: typical defects, detection approaches, and multisensor data fusion-based model. *The International Journal of*

Advanced Manufacturing Technology, 117(3):707–727, November 2021. ISSN 1433-3015. doi: 10.1007/s00170-021-07807-8. URL https://doi.org/10.1007/s00170-021-07807-8. 6

[15] Tobias Hauser, Adrien Da Silva, Raven T. Reisch, Joerg Volpp, Tobias Kamps, and Alexander F. H. Kaplan. Fluctuation effects in Wire Arc Additive Manufacturing of aluminium analysed by high-speed imaging. *Journal of Manufacturing Processes*, 56: 1088–1098, August 2020. ISSN 1526-6125. doi: 10.1016/j.jmapro.2020.05.030. URL https://www.sciencedirect.com/science/article/pii/S1526612520303455. 6

[16] Tobias Hauser, Raven T. Reisch, Philipp P. Breese, Benjamin S. Lutz, Matteo Pantano, Yogesh Nalam, Katharina Bela, Tobias Kamps, Joerg Volpp, and Alexander F. H. Kaplan. Porosity in wire arc additive manufacturing of aluminium alloys. *Additive Manufacturing*, 41:101993, May 2021. ISSN 2214-8604. doi: 10.1016/j.addma.2021.101993. URL https://www.sciencedirect.com/science/article/pii/S2214860421001585. 6

[17] Bintao Wu, Zengxi Pan, Donghong Ding, Dominic Cuiuri, Huijun Li, Jing Xu, and John Norrish. A review of the wire arc additive manufacturing of metals: properties, defects and quality improvement. *Journal of Manufacturing Processes*, 35:127–139, October 2018. ISSN 1526-6125. doi: 10.1016/j.jmapro.2018.08.001. URL https://www.sciencedirect.com/science/article/pii/S1526612518310739. 6

[18] Yongzhe Li, Xinlei Li, Guangjun Zhang, Imre Horváth, and Qinglin Han. Interlayer closed-loop control of forming geometries for wire and arc additive manufacturing based on fuzzy-logic inference. *Journal of Manufacturing Processes*, 63:35–47, March 2021. ISSN 1526-6125. doi: 10.1016/j.jmapro.2020.04.009. URL https://www.sciencedirect.com/science/article/pii/S152661252030219X. 6

[19] Jan Franke, Florian Heinrich, and Raven T. Reisch. Vision based process monitoring in wire arc additive manufacturing (WAAM). *Journal of Intelligent Manufacturing*, 36 (3):1711–1721, March 2025. ISSN 1572-8145. doi: 10.1007/s10845-023-02287-x. URL https://doi.org/10.1007/s10845-023-02287-x. 6, 9, 47

[20] Yuxing Li, Joseph Polden, Zengxi Pan, Junyi Cui, Chunyang Xia, Fengyang He, Haochen Mu, Huijun Li, and Lei Wang. A defect detection system for wire arc additive manufacturing using incremental learning. *Journal of Industrial Information Integration*, 27:100291, May 2022. ISSN 2452-414X. doi: 10.1016/j.jii.2021.100291. URL https://www.sciencedirect.com/science/article/pii/S2452414X21000881. 6

[21] Chunyang Xia, Zengxi Pan, Yuxing Li, Ji Chen, and Huijun Li. Vision-based melt pool monitoring for wire-arc additive manufacturing using deep learning method. *The International Journal of Advanced Manufacturing Technology*, 120(1):551–562, May 2022. ISSN 1433-3015. doi: 10.1007/s00170-022-08811-2. URL https://doi.org/10.1007/s00170-022-08811-2. 6, 9

[22] Welding Camera | Welding Vision System | Welding Analysis, . URL https://www.cavitar.com/product/cavitar-welding-camera/. 6

[23] XVC-700 / 710 / 750 Welding Cameras Weld Camera, . URL https://www.xiris.com/weld-monitoring-cameras/xvc-700/. 6

[24] Badr M. Abdullah. Monitoring of Welding Using Laser Diodes. In *Semiconductor Laser Diode Technology and Applications*. IntechOpen, April 2012. ISBN 978-953-51-0549-7. doi: 10.5772/36232. URL https://www.intechopen.com/chapters/35934. 7, 26

[25] XVC-1000 / 1100 Welding Camera Weld Camera, . URL https://www.xiris.com/weld-monitoring-cameras/xvc-1000/. 7

[26] Cavitar C300 Welding Camera System, . URL https://intertest.com/products/cavitar-c300-welding-camera-system. 7

[27] InGaAs Cameras: The Basics, 1. URL https://www.teledynevisionsolutions.com/learn/learning-center/imaging-fundamentals/ingaas-cameras-the-basics/. 7

[28] Cameron Serles. How to Choose Between SWIR and NIR Cameras for your Weld Process? URL https://blog.xiris.com/blog/how-to-choose-between-swir-and-nir-thermal-cameras-for-your-weld-process. 7

[29] Yikai Zhang, Shengnan Shen, Hui Li, and Yaowu Hu. Review of in situ and real-time monitoring of metal additive manufacturing based on image processing. *The International Journal of Advanced Manufacturing Technology*, 123(1):1–20, November 2022. ISSN 1433-3015. doi: 10.1007/s00170-022-10178-3. URL https://doi.org/10.1007/s00170-022-10178-3. 8

[30] Kang Dong, Qiang Wu, Xunpeng Qin, Zeqi Hu, and Lin Hua. In-situ optical monitoring and analysis of weld pool based on machine vision for wire and arc additive manufacturing. *The International Journal of Advanced Manufacturing Technology*, 133 (9):4865–4878, August 2024. ISSN 1433-3015. doi: 10.1007/s00170-024-14003-x. URL https://doi.org/10.1007/s00170-024-14003-x. 8

[31] Jie Wang, Zhifen Zhang, Zijian Bai, Shuai Zhang, Rui Qin, Jing Huang, and Guangrui Wen. On-line defect recognition of MIG lap welding for stainless steel sheet based on weld image and CMT voltage: Feature fusion and attention weights visualization. *Journal of Manufacturing Processes*, 108:430–444, December 2023. ISSN 1526-6125. doi: 10.1016/j.jmapro.2023.10.081. URL https://www.sciencedirect.com/science/article/pii/S1526612523010368. 8

[32] KUKA KR 6-2 Robot, . URL https://www.robots.com/industrial-robots/kuka-kr-6-2. 11

[33] Fronius CMT 4000 - Robots Done Right, . URL https://robotsdoneright.com/Robotic-Equipment/Welders/Fronius-CMT-4000.html. 11

[34] FRONIUS VR 7000 OPERATING INSTRUCTIONS/SPARE PARTS LIST Pdf Download, . URL https://www.manualslib.com/manual/1736836/Fronius-Vr-7000.html. 11

[35] MIG/MAG welding torches for robotic welding, . URL https://www.fronius.com/en/welding-technology/product-information/mig-mag-robot-welding-torches. 11

[36] Home, . URL https://www.fortiusmetals.com. 11

[37] Robert McNeel & Associates. Rhinoceros 3D. URL https://www.rhino3d.com/en/napa/. 15

[38] Basler Lens C12-2524-25M | Basler Product Documentation, . URL https://docs.baslerweb.com/c12-2524-25m. 17, 20

[39] Bit Depth, . URL https://www.cambridgeincolour.com/tutorials/bit-depth.htm. 17

[40] Premium Lens C12-2524-25M | Basler AG, . URL https://www.baslerweb.com/en-us/shop/basler-lens-c12-2524-25m/. 20

[41] Camera Mounting Systems | H.H. Barnum, . URL https://www.hhbarnum.com/products/vision-and-rfid/camera-mounting-systems/. 24

[42] Yiming Wang, Chenrui Zhang, Jun Lu, Lianfa Bai, Zhuang Zhao, and Jing Han. Weld Reinforcement Analysis Based on Long-Term Prediction of Molten Pool Image in Additive Manufacturing. *IEEE Access*, 8:69908–69918, 2020. ISSN 2169-3536. doi: 10.1109/ACCESS.2020.2986130. URL https://ieeexplore.ieee.org/document/9057613. Conference Name: IEEE Access. 24

[43] Understanding Neutral Density Filters, . URL https://www.edmundoptics.com/knowledge-center/application-notes/optics/understanding-neutral-density-filters/. 24

[44] George P. Masse. How Bright Is A Welding ARC In Lumens? - Weld Minds, March 2024. URL https://www.weldminds.com/how-bright-is-a-welding-arc-in-lumens/. Section: Guide. 24

[45] Zhuang Zhao, Lisheng Deng, Lianfa Bai, Yi Zhang, and Jing Han. Optimal imaging band selection mechanism of weld pool vision based on spectrum analysis. *Optics & Laser Technology*, 110:145–151, February 2019. ISSN 0030-3992. doi: 10.1016/j.optlastec.2018.08.058. URL https://www.sciencedirect.com/science/article/pii/S0030399218311423. 26

[46] Constant Current vs Constant Voltage Output, . URL https://www.lincolnelectric.com/en/welding-and-cutting-resource-center/process-and-theory/constant-current-vs-constant-voltage-output. 28

[47] Heat Input Calculators, . URL https://www.colliewelding.com/hicalculators.php. 28

[48] Amazon.com: Goreit Flashlight High Lumens Rechargeable, 990,000 Lumen Led Flashlights XHP70.2 USB Super Bright Flash Light Battery Powered, Powerful Handheld Flashlights for Emergencies Camping, IP67 Waterproof, . URL https://www.amazon.com/Flashlight-Rechargeable-Goreit-Flashlights-Emergencies/dp/B09SB8BN54?th=1. 41

[49] Ultralytics. YOLOv8. URL https://docs.ultralytics.com/models/yolov8. 47

[50] Mukesh Chandra, Sonu Rajak, and Vimal K.e.k. Deep learning-based framework for the observation of real-time melt pool and detection of anomaly in wire-arc additive manufacturing. *Materials and Manufacturing Processes*, 39(6):761–777, April 2024. ISSN 1042-6914. doi: 10.1080/10426914.2023.2254386. URL https://www.tandfonline.com/doi/full/10.1080/10426914.2023.2254386. Publisher: Taylor & Francis. 47

[51] Use Roboflow Annotate | Roboflow Docs, October 2024. URL https://docs.roboflow.com/annotate/use-roboflow-annotate. 47

[52] Limeng Pu, Rui Tian, Hsiao-Chun Wu, and Kun Yan. Novel object-size measurement using the digital camera. In *2016 IEEE Advanced Information Management, Communicates, Electronic and Automation Control Conference (IMCEC)*, pages 543–548, October 2016. doi: 10.1109/IMCEC.2016.7867270. URL https://ieeexplore.ieee.org/abstract/document/7867270. 47

Vita

Steven Grant Wilmoth is a Master's student at the University of Tennessee studying mechanical engineering. He is originally from Kingsport, Tennessee. His thesis is written on low-cost monitoring solutions for wire-arc additive manufacturing. He started college as an undergraduate student at the University of Tennessee in 2018 and graduated with a bachelor's in mechanical engineering in May of 2023. He will be graduating with his Master's in May of 2025.